Study on Short-Term Forecast of Localized Heavy Rainfall Based on the Statistical Characteristics of Cumulonimbus Clouds Observed by Ka-band Doppler Radars

March 2021

Syo YOSHIDA

Study on Short-Term Forecast of Localized Heavy Rainfall Based on the Statistical Characteristics of Cumulonimbus Clouds Observed by Ka-band Doppler Radars

A Dissertation Submitted to
the Graduate School of Life and Environmental Sciences,
the University of Tsukuba
in Partial Fulfillment of the Requirements
for the Degree of Doctor of Philosophy in Science
(Doctoral Program in Geoenvironmental Sciences)

Syo YOSHIDA

Abstract

Recently, it has been focused on the disasters caused by severe weather phenomena in Japan. Typhoons and quasi-stationary band-shaped precipitation systems can be forecasted several days and hours ago, respectively by numerical weather prediction (NWP) models based on the equation of motion. However, meso-γ-scale (spatial scale 2–20 km) cumulonimbus clouds causing localized heavy rainfall and urban floods, can develop so quickly that it is difficult to forecast with NWP models. The lead time for the heavy rainfall is about 20 minutes after being detected by operational centimeter-wavelength (X-, C-, or S-band) weather radars. To detect such clouds with greater lead times, Ka-band radars at a wavelength of 8.6 mm together with operational X-band radars were used in this study.

The beam width of Ka-band radars is very narrow (0.31°). However, since the elevation interval of the plan position indicators (PPIs) is much larger than the beam width, interpolation gaps are severe in the constant altitude PPI (CAPPI). Therefore, to fill these gaps and utilize the CAPPI data at all levels, the vertically averaged reflectivity (VAR) was calculated from the CAPPI of radar reflectivity Z. By adopting VAR, a continuous distribution of Z was obtained.

For statistical analyses of each cumulonimbus cloud, the algorithm for the

identification and tracking of convective cells (AITCC) was used to detect and track cloud. The AITCC extracts the regions enclosed by contour lines at a certain threshold of VAR. They were denoted as convective cell groups (CCGs). The characteristic of CCGs, such as area and maximum/averaged VAR in CCGs, are calculated. The process of tracking CCGs is as follows: 1) the average movement vector (MV) of all CCGs is calculated by the cross-correlation method using radar echoes at successive time steps, 2) the MV for individual CCGs is identified by linking the past and current CCGs using the average MV. If there are multiple links to one CCG, the similarity is evaluated based on the area, shape, and reflectivity (maximum and average) between the past and current CCGs. The CCGs for Ka-band and X-band radars were defined as mesoscale cloud echoes (MCEs) and mesoscale precipitation echoes (MPEs), respectively. The thresholds of VAR were –20 dBZ for MCEs, and 5 dBZ for MPEs. The upper limit of the MCE/MPE area (400 km^2) was also defined to focus on the cumulonimbus clouds. The MCEs which grew to MPEs were denoted as "developed MCEs" and which dissipated without developing into MPEs were denoted as "non-developed MCEs".

For case studies, four local heavy rainfall events that occurred in 2016 and 2017 were selected. They are local heavy rainfall events as rainfall with an intensity of 50 mm h^{-1} observed within 30 minutes of its onset. There were 15 developed MCEs and 39 non-

developed MCEs in total. In all cases, the local heavy rainfall occurred in the target domains after the convergence of sea breezes from the east and south. This is the typical conditions when the local heavy rainfall occurs around Tokyo.

The time series of each echo was analyzed by an echo tracking algorithm. On average, developed MCEs were detected 17 minutes earlier than the MPEs and 33 minutes earlier than the peak time of the area-averaged VAR (VARa) for MPEs. There were statistically significant differences between the developed and non-developed MCEs in terms of the maximum VARa (MaxVARa), maximum MCEs areas (MaxAREA), and increase amounts of the VARa (ΔVARa) and MCE areas (ΔAREA) for the elapsed time Δt = 6, 9, and 12 minutes, which is the time after the first detection of the MCE. To obtain the optimal indicator and its threshold, threat score (TS) for the prediction of MPEs was calculated. There is a trade-off between TSs and Δt, so that it is difficult to declare the best indicator. Nevertheless the MaxVARa produces TS of greater than 80 % and thus provides reliable predictions. Therefore, the MaxVARa for Δt = 9 minutes (threshold: 0 dBZ) would be the best indicator for practical forecasting. This indicator was obtained by limited cumulonimbus clouds triggered by the convergence of sea breeze around Tokyo. However, the thresholds and Δt are consistent with previous studies and have been shown to be applicable regardless of convective cloud type or

region of occurrence.

Nowcasting model for predicting MCE development was proposed using the above indicator. This model is expected to forecast rainfall earlier than conventional X-band radars, although there are following restrictions on its use; 1) this indicator is only applicable to convective echoes formed near Ka-band radar sites because the minimum detectable reflectivity decreases with the distance from radar sites due to attenuation, 2) the target of this model is limited to isolated cumulonimbus clouds, which are relatively unaffected by precipitation attenuation, 3) it is difficult to quantitatively forecast the rainfall amount caused by MCE whose development is predicted by this indicator. Forecasted MCEs have the potential for rainfall, but they do not always cause localized heavy rainfall. In order to forecast local heavy rainfall based on this indicator, it is necessary to examine the MCEs that occur around such precipitation systems.

Keywords: thunderstorm, Ka-band radar, short term forecasting

Contents

List of Tables

List of Figures

1. Introduction

Recently, it has been focused on the disasters caused by severe weather phenomena in Japan. For example, strong winds and heavy rainfall caused by typhoons. In case of Typhoon 1112 (TALAS), 50 stations reported that 24-hour rainfall broke the previous records. MLIT (Ministry of Land, Infrastructure, Transport and Tourism) reported that this typhoon also caused landslides, submergence and floods (MLIT 2011). In case of Typhoon 1919 (HAGIBIS), many stations reported that 3, 6, 12, and 24-hour rainfall broke the previous records in Shizuoka, Niigata, Kanto, and Tohoku regions. This typhoon also caused strong wind. The maximum instantaneous wind speed exceeded 40 ms^{-1} at seven stations in the Kanto region.

Localized heavy rainfall events producing accumulated three-hour precipitation amounts larger than 200 mm often cause severe landslides and floods. Such events are mainly brought by quasi-stationary band-shaped precipitation systems, named “senjo-kousuitai” in Japanese (Kato, 2020). Senjo-kousuitai is defined as a band-shaped heavy rainfall area with a length of 50–300 km and a width of 20–50 km, produced by successively formed and developed convective cells, lining up to organize multi-cell cluster, and passing or stagnating at almost the same place for a few hours. They occur frequently in the Pacific Ocean side of western Japan and the western side of Kyusyu

Island. In July 2020, heavy rainfall occurred in the western and eastern Japan, due to the stationary front (MLIT 2020).

Meso-γ-scale (spatial scale 2–20 km) cumulonimbus clouds occur in summer season are also hazardous. They cause localized heavy rainfall, but if they occur in an urban area, even over a short time, it can result in flooding. On 5 August 2008, the multi-cellular storm caused localized severe rainfall over the Zoshigaya area of Tokyo, and resulted in five sewer workers being swept away by a flash flood (Kato and Maki 2009; Hirano and Maki 2010). Similarly, on 28 July 2008, localized heavy rainfall caused rapid increasing in the water level of the Toga River in Hyogo, and children on the riverbank were swept away. The maximum 10-minute rainfall amount recorded at the Nagamine station of MLIT (135.220°E, 34.726°N) was 17.5 mm. Typhoons and senjo-kousuitai can be forecasted several days and hours ago, respectively, by numerical weather prediction (NWP) models based on the equation of motion. However, meso-γ-scale cumulonimbus clouds develop so quickly that it is difficult to forecast with NWP models. They often occur heavy rainfall only 20 minutes after detected by conventional (S-, C-, or X-band) weather radars (Ishihara 2012; Kim et al. 2012). Therefore, it is important to detect cumulonimbus clouds as early as possible for flood warning systems.

Recently, operational X-band radars have been used in Japan to observe

cumulonimbus clouds in urban areas. MLIT installed an extended radar information network (XRAIN) consisting of 39 X-band (wavelength of about 3 cm) multi-parameter (MP-X) radars. XRAIN can obtain the distribution of rainfall intensity at the surface every minute in major urban areas and can perform a volumetric scan every 5 minutes. Nowcasts (short-term precipitation forecasts using XRAIN) based on the vertically integrated liquid (VIL) water content (Hirano and Maki 2010, 2018), vertical vorticity estimated from Doppler velocity (Nakakita et al. 2013), and tracking algorithms for precipitation systems (Yoshida et al. 2012) have been proposed. In recent years, X-band phased array weather radars (PAWRs), which can obtain a three-dimensional observation within 30 seconds, have been developed (Yoshikawa et al. 2013; Yoshida et al. 2013; Ushio et al. 2015). More recently, a polarimetric PAWR has been developed (Takahashi et al. 2019). The fast observation by PAWRs makes it possible to capture the detailed vertical structure of rapidly developing cumulonimbus clouds. A nowcasting model based on PAWRs that includes vertical advection has also been proposed (Otsuka et al. 2016).

In current operational nowcasting models, extrapolation of radar echoes is the primary mechanism, so the forecast can be updated frequently. On the other hand, the prediction accuracy decreases sharply during the 0 to 1 hour forecast window with a

rate closely related to the scale of the precipitation pattern and the associated forcing mechanism (Wilson et al. 1998). Hirano et al. (2018) proposed a nowcasting model that considers time changes based on initial values, but the decrease in prediction accuracy is remarkable. To solve this problem, there are previous studies that blend the time extrapolation-based nowcasting model with the NWP model (Radhakrishnan and Chandrasekar 2020; Kato et al. 2017). The update frequency of typical NWP models is less than that of time extrapolated nowcasting models, but it is possible to forecast precipitation that does not exist at the initial time. Radhakrishnan and Chandrasekar (2020) blended the US Dynamic and Adaptive Radar Tracking of Storms (DARTS) nowcasting model (Ruzanski et al. 2011) with the WRF model (1 km grid). They showed that the prediction accuracy for 30 minutes to 1 hour was improved compared with each model. Kato et al. (2017) compared the prediction accuracy of High-Resolution Precipitation Nowcasts (HRPNs) provided by the Japan Meteorological Agency (JMA) (Kigawa 2017a, 2017b) and a high-resolution (0.7 km) cloud-resolving storm simulator (CReSS) for each lead time. The prediction accuracy of HRPNs was higher up to 40 minutes, and CReSS was higher for 45 minutes to 1 hour. This suggests the possibility of seamless, high-accuracy forecasts of heavy rainfall by blending these models. Furthermore, there is the nowcasting model for meteorological radar images based on

the deep learning (Marrocu and Massidda 2020). They showed that the prediction accuracy up to 1 hour is improved over the conventional time extrapolation-based nowcasting model.

The main target of X-band radars such as MP-X and PAWR is precipitation particles. The X-band radar wavelength cannot be used to observe cloud droplets. To detect cumulonimbus clouds earlier, it is necessary to use millimeter-wave radars. The U.S. Department of Energy has acquired scanning Ka-band (wavelength of 8.5 mm) radars in the Atmospheric Radiation Measurement (ARM) Program (Kollias et al. 2014). Borque et al. (2014) showed the advantages of the ARM Ka-band radar for observing clouds without precipitation. The Korean Meteorological Administration also operates a scanning Ka-band radar in combination with microwave radiometers to study cloud water content estimation (Oh et al. 2018). A scanning Ka-band radar has also been developed in Japan (Hamazu et al. 2003) to observe fog (Uematsu et al. 2005) and the development of cumulonimbus clouds (Sakurai et al. 2012; Nishiwaki et al. 2013; Misumi et al. 2018a). Sakurai et al. (2012) showed that the Ka-band radar can detect the first echoes about 15 to 25 minutes earlier than X-band radars, and that a rapid increase of radar reflectivity could be an indicator of cumulonimbus development. Nakakita et al. (2017) showed that a Ka-band radar can predict the possibility of local

heavy rainfall more than 10 minutes earlier than X-band radars. Few studies have been conducted on short-term precipitation forecasts using millimeter-wave radars because these radars are easily affected by attenuation and it is difficult to apply them to scan the wide areas necessary for tracking the movement of echoes. Another important reason is that an operational network has not yet been deployed.

Recently, the National Research Institute for Earth Science and Disaster Resilience (NIED) has deployed five Ka-band radars in the Tokyo metropolitan area (Maesaka et al. 2015; Maesaka 2018). This radar network enables the tracking of convective echoes from the initial to the mature stages with a plan position indicator (PPI). The radar network reduces the influence of rain attenuation by observing one echo with multiple radars. The Ka-band radar network overlaps the XRAIN observation range, and thus different-wavelength radars can observe the formation and development of cumulonimbus clouds simultaneously.

Another problem in short-term precipitation forecasting using millimeter-wave radar is that it is not known whether the detected early radar echoes will develop into heavy precipitation echoes. The early stage echoes detected by millimeter-wave radars may dissipate without causing any precipitation on the ground. Therefore, an indicator is necessary to predict whether the detected radar echoes will develop.

The objectives of this study are as follows; 1) to investigate the statistical characteristics of the development of early echoes observed by Ka-band radar network, and 2) to propose the nowcasting model utilizing the characteristics above.

In this study, the radar reflectivity factor provided from Ka-band radar network installed by NIED was used for the analysis of cumulonimbus clouds in the early stages. XRAIN was also used for the analysis of those clouds in the developing and mature stages. The case studies consisted of local heavy rainfall events in the Tokyo metropolitan area in 2016 and 2017. The algorithm for the identification and tracking of convective cells (AITCC, Shimizu and Uyeda 2012) was used to obtain the statistical characteristics of individual convective echoes. Based on the results, the generality of the characteristics of the development of early echoes and the limitation of the proposed model are discussed.

2. Data

2.1. Ka-band radars

In this study, five Ka-band radars located at Tsukuba (TKB), Ota (OTA), Hanno (HNO), Nishitokyo (NTK), and Matsudo (MTD) were used. These radars were installed to cover densely populated areas in the Tokyo metropolitan area (Fig. 1). The analysis

domains correspond to the observation areas of HNO and NTK in 2016 and those of all five radars in 2017 (solid and dashed frames in Fig. 1).

The Ka-band radars use frequencies between 34.8 and 34.9 GHz and have a beam width of 0.31°. A pulse width of 55 μs (long pulse) is usually used with pulse compression technology to improve range resolution and sensitivity. However, such long pulses cannot be used to observe radar echoes within 8.7 km of a radar; this range is covered by short pulses (1.0 μs). The maximum observation range is 30 km and the range resolution is 150 m. The minimum detectable reflectivity is about −17 dBZ in dual-polarization mode (TKB, OTA, and HNO) and about −20 dBZ in single-polarization mode (NTK and MTD) at the 20-km distance. Each radar performs PPI observations at four to six elevation angles every 3 minutes (TKB: 5.2°, 8.0°, 11.5°, 15.7°, 20.8°, 27.2°; OTA: 1.6°, 4.5°, 7.5°, 10.6°, 15.0°; HNO: 5.0°, 7.0°, 10.5°, 14.9°, 20.3°; NTK: 6.8°, 10.3°, 14.4°, 19.5°, 26.21°; MTD: 2.7°, 5.8°, 10.0°, 16.4°). The outputs are the radar reflectivity (Z), Doppler velocity (V), and spectrum width (W) for NTK and MTD, and the differential reflectivity (Z_{DR}), specific differential phase (K_{dp}), and correlation coefficient (ρ_{hv}), as well as Z, V, and W, for the other radars. The specifications of the Ka-band radars are listed in Table 1.

2.2. Radar reflectivity

Weather radars are often used to show the locations of storms. Most radars are capable of not only detecting storms, but they are also capable of measuring the strength of the returned power which in turn can be used to estimate rainfall rate and other parameters of the storms (Fukao and Hamazu 2009).

When discrete small size targets like raindrops and cloud droplets are distributed, the radar equation is

$$P_r = \frac{\pi^3 P_t G^2 \theta^2 c\tau |K|^2}{10^{18} 2^{10} (\ln 2) \lambda^2} \cdot \frac{1}{r^2} \cdot Z \tag{2.1}$$

where P_r is the received power (W), P_t is the transmitted power (W), G is the antenna gain, θ is the beam width (°), c is the speed of light (m s^{-1}), τ is the pulse width (μs), λ is the wavelength (m), r is the range between the radar and the targets (m). $|K|$ is a parameter related to the complex index of refraction of the material given by

$$|K| = \left| \frac{\varepsilon - \varepsilon_0}{\varepsilon + 2\varepsilon_0} \right| \tag{2.2}$$

where ε and ε_0 are conductivities of raindrops and atmosphere. Z is the radar reflectivity factor (mm^6 m^{-3}) given by

$$Z = \int_0^\infty N(D) D^6 dD \tag{2.3}$$

where D is the rain drops of diameter (m), $N(D)$ is the number of diameter of droplets. For the dual-polarization radars, radar reflectivity factors are determined from each polarization, giving Z_H and Z_V.

Rainfall rate R can be estimated with the relationship between radar reflectivity and R (Z-R relationship). The most commonly used relationship is the empirical power-low relationship

$$Z = aR^b \tag{2.4}$$

where parameters a and b are variable because R depends on the drop size distribution (DSD) and DSD differs from precipitation. But many empirical values have been suggested in previous studies and for the most convective storms, Eq. (2.4) becomes

$$Z = 300R^{1.35} \tag{2.5}$$

for the most stratiform rainfall,

$$Z = 200R^{1.6} \tag{2.6}$$

is used (Fukao and Hamazu 2009).

Conventional radars sometimes underestimate rainfall rate because their signals are reduced in power by attenuation of strong rainfall. To get around this problem, multi-

parameter radars use the specific differential phase K_{dp} to detect raindrops which hardly get attenuation. K_{dp} is calculated from the differential phase ϕ_{dp}, as will be explained later.

2.3. Differential reflectivity

The differential reflectivity Z_{DR} is the difference between Z_H and Z_V. Z_{DR} is defined as follows:

$$Z_{DR} = 10 \log_{10} \left(\frac{Z_H}{Z_V} \right) \tag{2.7}$$

Z_{DR} varies from near zero for spherical droplets to values as large as +5 dB for echoes from large water drops. This is useful for refining rainfall measurements made by radar. Z_{DR} is also useful for indicating the presence of hail. In the presence of strong reflectivity, Z_{DR} from raindrops should be moderately large. However, in the presence of hail, Z_{DR} often close to zero, because the hailstones generally tumble as they fall.

2.4. Differential phase

Since falling raindrops are not sphere, the phase of horizontal signal start to lag earlier than the vertically polarization signal. This produces a slight change in phase

between the two signals. This lag is called the differential phase ϕ_{dp}, and its magnitude depends on both the orientation as the hydrometeors fall and the total path length to the targets. ϕ_{dp} can be defined by the following equation:

$$\phi_{dp} = \phi_{hh} - \phi_{vv} \tag{2.8}$$

where ϕ_{hh} and ϕ_{vv} represent the phase change of horizontal and vertical signals, respectively. Generally, ϕ_{hh} is larger than ϕ_{vv}, because falling rain drops are flattened.

2.5. Specific differential phase

The specific differential phase K_{dp} is the rate of change of the differential phase. K_{dp} is defined as follows:

$$K_{dp} = \frac{\phi_{dp}(r_2) - \phi_{dp}(r_1)}{2(r_2 - r_1)} \tag{2.9}$$

K_{dp} is used to calculate rainfall rate, because K_{dp} is one half of the range derivative of the two differential phase and less affected by the attenuation by strong rainfall than the radar reflectivity. The example of rainfall estimator is the following equation which Park et al. (2005) proposed.

$$R = \begin{cases} 7.07 \times 10^{-3} Z^{0.819} & K_{dp} \le 0.3^{\circ}\mathrm{km}^{-1} \\ & or\ 10\log Z \le 35\mathrm{dBZ} \\ 19.63 {K_{dp}}^{0.823} & otherwise \end{cases} \tag{2.10}$$

This estimator is different for strong and weak rainfall with thresholds of 35 dBZ and $0.3°km^{-1}$.

2.6. Correlation coefficient

The correlation coefficient ρ_{hv} is the correlation between the horizontally and vertically polarized signals at a given point in space at the same time. ρ_{hv} is defined as follows:

$$\rho_{hv} = \frac{\langle S_{vv} S_{hh}^{*} \rangle}{\langle |S_{hh}|^2 \rangle^{1/2} \langle |S_{vv}|^2 \rangle^{1/2}} \tag{2.11}$$

where, s and s^{*} are scattering matrices, and subscripts h and v represent the received and transmitted polarizations for horizontal and vertical signals, respectively. The magnitude of the ρ_{hv} depends upon the targets being measured. For perfect spheres, $\rho_{hv} = 1.0$. However, in the case of rain, ρ_{hv} is close to 1.0 but not quite. It usually takes the value of 0.97 to 0.99, depending upon how hard it is raining. Irregular shaped hydrometeors (i.e., ice crystals, hail, snow, or graupel) or noise decrease ρ_{hv}.

2.7. Doppler velocity

Doppler velocity is the radial velocity of target deduced by phase shifting of received

signal due to difference of radar transmitted frequency and received frequency. Suppose radio wave was transmitted from a radar with transmitted wavelength λ and the distance between the radar and the target is r, relationship between initial phase of transmitted signal φ_0 and the phase of received signal φ is expressed as follows:

$$\varphi = -\frac{4\pi r}{\lambda} + \varphi_0 \tag{2.12}$$

Furthermore, time variation of phase is:

$$\frac{d\varphi}{dt} = -\frac{4\pi}{\lambda}\frac{dr}{dt} \tag{2.13}$$

where $v_d = dr/dt$ is the Doppler velocity. Additionally, time variation term (left-hand) called as Doppler angular frequency ω_d. It also expressed by $\omega_d = 2\pi f_d$ using Doppler frequency sift f_d. Consequently, Doppler velocity v_d is expressed as follows:

$$\omega_d = 2\pi f_d = -\frac{4\pi}{\lambda} v_d \tag{2.14}$$

2.8. Nyquist velocity

There is limitation in the velocity that a radar can resolve unambiguously and this limitation is called Nyquist velocity. If the velocity exceeds Nyquist velocity, the velocity aliasing occurs (Fukao and Hamazu 2009).

The maximum velocity a Doppler radar can detect correctly or unambiguously is given by the velocity which produces a phase shift of ±π radians. Mathematically, the maximum velocity can be express as

$$v_N = \frac{\pm f_{max}\lambda}{2} \tag{2.15}$$

The maximum frequency f_{max} is given by

$$f_{max} = \frac{PRF}{2} \tag{2.16}$$

where PRF is the pulse repetition frequency of the radar. Thus, the maximum unambiguous velocity detectable by a Doppler radar is

$$v_{max} = \frac{\pm PRF\lambda}{4} \tag{2.17}$$

If the velocity aliasing occurs, the aliased velocity is expressed as

$$v_r = v_d \pm 2Nv_N \tag{2.18}$$

where N is called Nyquist number.

2.9. Quality control for Ka-band radars

To remove non-meteorological echoes (such as insects), it was considered the cloud

echoes when the 5 bins × 5 rays moving average of the received power ($\overline{P_r}$) was larger than a certain noise level:

$$\overline{P_r} = 10\log\left(\sum_{-2\le ray\le 2}\sum_{-2\le bin\le 2} 10^{\frac{P_r}{10}}\right) \ge noise\ level \tag{2.19}$$

This procedure is adopted because the spatial fluctuations differ between meteorological and non-meteorological echoes. Polarimetoric methods (e.g., ρ_{hv} thresholding) would be more reliable, but two of the five Ka-band radars are non-polarimetric and these methods were not applied in this study. The noise level in Eq. 1 was calculated by adding the dispersion (4 dB) to the average value of the received power for a clear sky. The noise levels are approximately ≤ −110 dBm for short pulses and ≤ −123 dBm for long pulses, though the values slightly vary with radar. Furthermore, data that included spurious echoes such as range side lobes and second trips were excluded.

2.10. Attenuation correction for Ka-band radars

In general, Ka-band radars are strongly affected by attenuation because of their short wavelengths compared to those of conventional weather radars. Here, attenuation correction for the atmosphere was performed by assuming an attenuation rate of 0.15

dB km^{-1} (one way). This value is based on the results of the millimeter-wavelength propagation model (Liebe 1985). Generally, the specific attenuation depends on temperature and humidity, so it is necessary to consider their time and space variations for accurate correction. However, it is difficult to obtain their temporal and spatial distributions within the observation range. Therefore, the correction was made using a constant value.

Attenuation corrections for Ka-band reflectivity for precipitation particles or cloud droplets have been proposed using dual-wavelength radars (Chandrasekar et al. 2003), a vertical pointing radar (Matrosov 2005), and dual Ka-band radars (Nishikawa et al. 2016). However, the main target of this study is early convective echoes, which appear in environments where the attenuation due to other convective echoes is negligible. Moreover, the networked Ka-band radars reduce the influence of attenuation by observing one cumulonimbus cloud with multiple radars. Therefore, no correction was made for precipitation particles or cloud droplets.

2.11. X-band radars

To analyze precipitation echoes, five operational X-band radars, respectively located at Saitama (SAI), Shin-Yokohama (SYK), Funabashi (FNB), Yattajima (YAT), and Ujiie

(UJI), were also used. Their minimum detectable reflectivity is about 2 dBZ (SAI), 5 dBZ (SYK), and 10 dBZ (FNB, YAT, and UJI, respectively) at a 30-km distance. The maximum observation range of these radars is 80 km and their range resolution is 150 m. PPI observations at 12 elevation angles are routinely performed every 5 minutes, where the two underlined elevation angles listed below are scanned alternately every minute to estimate the rainfall intensity at the surface (SAI: 1.4°, 2.4°, 0.8°, 3.6°, 4.9°, 6.3°, 7.9°, 9.7°, 11.8°, 14.2°, 16.9°, 20.0°; SYK: 1.7°, 2.6°, 1.0°, 3.8°, 5.1°, 6.5°, 8.1°, 9.9°, 11.9°, 14.2°, 16.9°, 20.0°; FNB: 1.6°, 2.6°, 0.6°, 3.8°, 5.1°, 6.5°, 8.1°, 9.9°, 11.9°, 14.2°, 16.9°, 20.0°; YAT: 1.6°, 2.7°, 0.5°, 3.9°, 5.2°, 6.6°, 8.2°, 10.0°, 12.0°, 14.2°, 16.8°, 20.0°; UJI: 1.4°, 3.0°, 0.7°, 2.2°, 4.2°, 5.6°, 7.2°, 9.1°, 11.3°, 13.8°, 16.7°, 20.0°). The products of these radars are Z, V, W, Z_{DR}, K_{dp}, and ρ_{hv}. Table 2 lists the specifications of the X-band radars. Detailed quality control methods of the X-band radars, including attenuation correction, are shown in Maesaka et al. (2011).

3. Methodology

3.1. Conversion the coordinates

The PPI obtained at each radar site was converted to a constant altitude PPI (CAPPI) of Z using the Cressman interpolation method (Cressman, 1959). In the radar data, the

sampling volume becomes large as data point is far from the radar site. Therefore, effective radius of sphere used for the Cressman interpolation is changed according to the distance from radar. The effective radius is defined as follows:

$$R_H = ar + b \tag{3.1}$$

where R_H is the effective radius and $a = 5.411 \times 10^{-3}$, $b = 0.0$. Cressman interpolation is expressed as:

$$V = \frac{\sum_i W_i v_i}{\sum_i W_i} \tag{3.2}$$

where V is the value at interpolation point, v_i is the observed value and W_i is the weight for the interpolation. The W_i is defined as follows:

$$W_i = \left(1 + \frac{d^3}{{R_H}^3}\right)^{-1} \tag{3.3}$$

where, d is the distance between grid point and observed data point. After interpolation, horizontal smoothing with a 3 × 3 mesh median filter was applied. For grids which could not be interpolated by available data, a 5 × 5 mesh Gaussian filter was applied. For Ka-band radars, the horizontal and vertical grid resolutions for the interpolation were 150 and 100 m, respectively, considering the beam spread (162 m) at 30 km from the radar. For X-band radars, horizontal and vertical grid intervals are 500

and 250 m, respectively.

3.2. Vertically averaged reflectivity

According to the CAPPI of Z for Ka-band radars (Fig. 2a and Fig. 2b), the interpolation gaps are conspicuous, because the interval of the elevation angles is large compared to the beam width. Therefore, to fill these gaps and utilize the reflectivity at all levels, the vertically averaged reflectivity (VAR) was calculated from the CAPPI data as

$$VAR_{ij} = 10\log\left(\frac{1}{n}\sum\nolimits_{k} Z_{ijk}\right) \tag{3.4}$$

where the subscripts i, j, and k represent the grid points along the x, y, and z axes of the CAPPI data, respectively, Z_{ijk} is the radar reflectivity at (i, j, k) ($mm^6\ m^{-3}$), and n is the number of vertical grids where $Z_{ijk} > 0$ at (i, j). The unit of the VAR is dBZ. By adopting VAR, a continuous horizontal distribution for the reflectivity was obtained (Fig. 2c). However, because VAR projects three-dimensional information onto a horizontal plane, it should be noted that the data at different elevations may be mixed in each horizontal grid. The number of PPIs that contribute to VAR varies depending on the distance from the radar; it is more than 10 in the analysis domains (Fig. 2d). VAR is similar to VIL, which was not used in this study because it is difficult to obtain the

cloud-water content from the reflectivity of a Ka-band radar, especially when drizzle is present (Khain et al. 2008). Similar to Ka-band radars, VAR for X-band radars was also calculated.

3.3. Definition of echoes

For the statistical analysis, radar echoes were classified as follows. In the VAR derived from Ka-band radars, if an area enclosed by a contour line of −20 dBZ was between 3 to 400 km^2, these echoes are denoted mesoscale cloud echoes (MCEs). For X-band radars, the threshold for the VAR was set to 5 dBZ and the echoes are denoted mesoscale precipitation echoes (MPEs). These thresholds almost correspond to the minimum detectable reflectivity for both radars. The MCE and MPE areas were automatically calculated by the AITCC by counting the number of grids within the outermost contours. The upper limit of the MCE (MPE) area was defined to exclude echoes larger than the meso-γ-scale (2 to 20 km). However, there were no such large echoes in this study. The lower limit of the area was defined to exclude non-precipitation echoes such as ground clutter, which could not be removed by the moving target indication (MTI) method. The MCEs that developed into MPEs are denoted as developed MCEs and those that did not develop into MPEs are denoted as non-developed MCEs in this paper.

3.4. Detection and tracking of echoes

The AITCC was used for the detection and tracking of MCEs and MPEs. This algorithm identifies individual convective cells (CCs) and their groups (convective cell groups, CCGs). First, the AITCC extracts the regions enclosed by contour lines at a certain threshold of reflectivity. The region is defined as a CCG. Then, the CCG is divided into CCs, which consist of a single reflectivity peak and its surrounding areas. In the present study, CCGs derived from the VAR are defined as MCEs or MPEs. They were detected every 3 and 5 minutes, respectively.

The CCG tracking method in the AITCC is as follows. First, the average movement vector (MV) of all CCGs is calculated by the cross-correlation method using radar echoes at successive time steps. Next, the MV for individual CCGs is identified by linking the past and current CCGs using the average MVs. If there are multiple links to one CCG, the similarity is evaluated based on the area, shape, and reflectivity (maximum and average) between the past and current CCGs. If there are multiple CCGs with high similarity, they are determined to be merged/separated. In this study, the tracking results were manually checked; when the characteristics of an MCE (MPE) at a certain time differed significantly from those at the previous time step, they were treated as the formation of a new MCE or MPE. In addition, the MCEs (MPEs) that formed or extended

outside of the study area, or which dissipated within two time steps, were excluded from the analysis. The example of the MCE detection/tracking results obtained with the AITCC was shown in Fig. 3.

4. Analysis period

The local heavy rainfall events were selected that occurred in the study area in August 2016 and 2017. Nakakita et al. (2016) defines a local heavy rainfall event as rainfall with an intensity of 50 mm h^{-1} observed within 30 minutes of its onset. In 2016 and 2017, there were four local heavy rainfall events in the study area (Table 3). All of the cases were in August because deep convection frequently occurs under weak synoptic-scale forcing in the study area. The surface weather maps and sounding data from Tateno (140.125°E, 36.057°N) on each event are shown in Fig. 4 to Fig. 7.

On 4 August 2016 (CASE1, Fig. 4), eastern Japan was covered with high pressure and cleared up in the morning, but there was a heavy local thunderstorm in the afternoon. The sounding data at 1200 Japan Standard Time (JST, UTC+9) shows a relatively dry lower layer (below the 933-hPa level), with the relative humidity (RH) increasing with height, and also shows a dry layer above the isotherm layer. The RH were 75 % and 86 % at the lowest layer (1008 hPa) and 933 hPa, respectively. The 0°C isotherm was

situated at 555 hPa, about 5 km. The level of free convection (LFC) was 2.9 km for a parcel from the lowest 500 m of the atmosphere, and equilibrium level (EL) was 12.7 km. The amount of precipitable water (PW) for entire sounding was 47.6 mm, and convective available potential energy (CAPE) was 839.4 J kg^{-1}. According to the XRAIN radar observations, two small-scale echoes appeared in the study area (black dashed frame in Fig. 8a), and caused 26.5 mm for total rainfall amount.

On 9 August 2017 (CASE2, Fig. 5), due to the Typhoon 1705 (NORU), which changed into an extratropical cyclone in the Sea of Japan, the temperature in the Kanto region increased. The atmospheric condition at 0900 JST was similar to CASE1, but the RH increased with height from 903 hPa to 715 hPa (RH were 65 % and 89 %, respectively). The 0°C isotherm was situated at 492 hPa, about 5.9 km. The LFC and EL were 1.9 km and 14.5 km, which were lower / higher than CASE1. The PW was 57.6 mm and CAPE was 1051.2 J kg^{-1} (the maximum value in the four cases). Similar to CASE1, localized echoes appeared in the study area and caused 49.2 mm for total rainfall amount (Fig. 8b).

On 19 August 2017 (CASE3, Fig. 6), the lower layer below 900 hPa was humid. RH below this altitude was above 90 %. The 0°C isotherm was situated at 566 hPa, about 4.9 km. The LFC and EL were 2.5 km and 11.4 km, respectively. The PW was 55.6 mm

and CAPE was 743.7 J kg^{-1}. The localized storm developed in the study area, which cause total rainfall amount of 80.5 mm (Fig. 8c).

The precipitation event on 30 August 2017 (CASE4, Fig. 7) was caused by a stationary front. The surface weather map for 0900 JST shows a stationary front lying on the target area. The 0°C isotherm was situated at 540 hPa, about 5.3 km. The LFC and EL were 1.6 km and 12.6 km, respectively. The PW was 54.4 mm and CAPE was 571.8 J kg^{-1}, which was the lowest CAPE in the four cases.

In these cases, local heavy rainfall occurred after the convergence of sea breezes from the east and south (Fig. 8). Such conditions are frequently observed when local heavy rainfall occurs around Tokyo (Fujibe et al. 2002; Saito et al. 2018). Therefore, the study cases are typical of convective events in the Tokyo metropolitan area.

5. Results

5.1. Characteristics of developed MCEs

In this section, the characteristics of MCEs are examined based on the time variation of the VAR. The horizontal distribution of VAR for developed MCEs observed in CASE1 is shown in Fig. 9. Two MCEs (M1, M2) were detected at 1403 JST, and another MCE (M3) formed to the east of M2 at 1412 JST. MPEs for M1 and M2 were detected at 1415

JST, and the MPE for M3 formed at 1420 JST. They continued to develop, reaching their peak VAR at 32 minutes after their first detection. The time series of the area-averaged VAR (VARa) of the MCEs and MPEs are shown in Fig. 10. The thresholds for the VAR of MCEs and MPEs are −20 and 5 dBZ, respectively, as described above. VAR varied about two orders of magnitude within a MCE (MPE) (unit: $mm^{-6}\ m^{-3}$), and VARa values were close to the 75th percentile of VAR in the early stages of MCEs (MPEs). The time differences (t_1) of the first detection between the MCE and MPE were 12 minutes for M1 and M2 and 8 minutes for M3, and the time differences (t_2) between the first detection of the MCE and the first VARa peak of the MPE (hereafter referred to as the peak time) were 32 minutes for M1 and M2 and 28 minutes for M3. At the time when the MCEs formed, their VARa values differed greatly (−13.5, −3.4, and −6.6 dBZ for M1, M2, and M3, respectively). However, the areas of initial MCEs were similar (4.6, 3.6, and 4.8 km^2, respectively). The areas increased to 20 km^2 when the MPEs were detected. In this case, six developed MCEs were detected.

Table 4 shows the characteristics of 15 developed MCEs in all cases. The mean values of t_1 and t_2 were 16.7 and 32.7 minutes, respectively. On average, the increase amount of VARa (ΔVARa) in the period between the first detection of MCEs and MPEs was 19.2 dB and the average of the maximum VARa (MaxVARa) during this period was 12.9 dBZ.

The average increment of the MCE areas (ΔAREA) was 27.4 km^2 and the average of the maximum MCE areas (MaxAREA) was 33.6 km^2 in this period.

5.2. Indicator of MCE development

In this section, the characteristics of developed MCEs are compared with those of non-developed MCEs to find an indicator to predict MCE development. There were 39 non-developed MCEs. The mean values of the initial VARa and the areas of these MCEs were −10.4 dBZ and 4.6 km^2, respectively, which are comparable to those of the developed MCEs (−8.6 dBZ and 6.2 km^2). Therefore, there is no significant difference at the initial stage of MCEs. However, the MaxVARa before the dissipation of MCEs was −3.7 dBZ on average, which is much smaller than that of the developed MCEs (12.9 dBZ before the detection of MPEs). Similarly, the MaxAREA was 8.5 km^2 on average for non-developed MCEs, which is smaller than that of the developed MCEs (33.6 km^2).

Here, the elapsed time (Δt) is defined as the time after the first detection of an MCE. The histograms of ΔVARa, MaxVARa, ΔAREA, and MaxAREA for Δt = 15 minutes are shown in Fig. 11. There are differences between the developed and non-developed MCEs in terms of these variables. The MaxVARa values show a clear difference; they are always greater than 0 dBZ for developed MCEs and always smaller than 5 dBZ for non-

developed MCEs. The mean values of the MaxVARa were 13.4 and −3.3 dBZ for the developed and non-developed MCEs, respectively. Differences are also clear for Δt = 9 minutes (Fig. 12), but not clear for Δt = 3 minutes (Fig. 13).

Table 5 shows the results of the Lepage test for Δt = 15, 12, 9, 6, and 3 minutes to examine whether the differences between the developed and non-developed MCEs were statistically significant. Except for some variables for Δt = 3 and 15 minutes, the differences were significant at the 99 % confidence level. Among them, the highest value is for the MaxVARa for Δt = 9 minutes. Table 6 shows the threat score (TS) for the prediction of MPEs using each indicator, where the thresholds for predicting developed and non-developed MCEs for each indicator were chosen to maximize the TSs. MCEs whose t_1 was less than Δt were excluded from the calculation of the TSs. The TSs are relatively high when the MaxVARa values were used as an indicator (57.1, 83.3, 90.0, and 85.7 % for Δt = 6, 9, 12, and 15 minutes, respectively). The TS is the highest for ΔAREA (58.8 %) when Δt = 3 minutes. The mean lead times to the first detection of MPEs are 13.7, 10.7, 7.7, 4.7, and 1.7 minutes for Δt = 3, 6, 9, 12, and 15 minutes, respectively. There is a trade-off between TSs and the lead time, which makes it difficult to declare the best indicator. Nevertheless the MaxVARa produces a TS of greater than 80 % and thus provides reliable predictions. Therefore, the MaxVARa for Δt = 9

minutes (threshold: 0 dBZ) would be the best indicator for practical forecasting.

5.3. Nowcasting model utilizing developmental indicator

In this section, a nowcasting model for predicting MCE development with the indicator obtained in the last section is proposed. Here, it is supposed that MCEs are detected based on the VAR field obtained from Ka-band radars at $t = t_0 - \Delta t$ (Fig. 14). The VARa values of the MCEs are calculated from this time. After a time period Δt, forecasting starts only for MCEs whose MaxVARa value exceeds a certain threshold at time $t = t_0$. The MVs are calculated using the movements of MCEs for $t = t_0 - \Delta t$ and t_0, and the locations of the MCEs are extrapolated to T minutes ahead along the MV (T is the lead time of this model). Finally, the potential occurrence regions of MPEs are forecast along the movement area of the MCEs.

This model aims to detect developing cumulonimbus clouds as early as possible and forecast their rainfall area. The time difference between the first detection of MCEs and MPEs is about 17 minutes, and that between the first detection of MCEs and the peak time of MPEs is about 33 minutes. Therefore, if Δt = 9 minutes is used, the lead time T for the detection of MPEs and their peak time will be 8 and 24 minutes, respectively. The model is also feasible to C or S-band radars instead of X-band radars. In such cases,

the lead time may vary depending on radar sensitivity.

6. Discussion

In the previous chapter, the indicator of MCE development (MaxVARa ≥ 0 dBZ for Δt = 9 minutes) and the nowcasting model utilizing this indicator were proposed. In this chapter, the generality of this indicator and the limitation of this model are discussed.

6.1. Generality of the indicator

In this study, cumulonimbus clouds initiated by updrafts associated with the local convergence of sea breezes were considered. The other types of convective clouds that develop under different conditions, such as orographically induced convection, have not been investigated. Unlike the case for the convergence of sea breezes, the updraft would be maintained for a relatively long time in mountainous areas, which may affect the VAR time variation. In this section, the generality of this indicator is discussed in terms of the precipitation formation process.

Precipitation particles in convective clouds that do not contain the ice phase (warm rain), are generated by the following two processes. That is, the condensation process and the collision-coalescence process. In the condensation process, cloud particles grow

by the condensation of surrounding water vapor. Since this growth rate is inversely proportional to the radius of the particles, the rate decreases as the growth progresses. The particles grow to several tens of micrometers in this process. Next, the grown particles collide and merge with the surrounding smaller particles (collision-coalescence process). In this process, the diameter of the particles increases explosively, eventually resulting in precipitation on the ground in many cases. While the particle size distribution is unimodal in the condensation process, it becomes bimodal in this process, which is the major feature of the precipitation process in warm rain. The developed MCEs are echoes under this process. According to the idealized experiment by Shiino (1986), the critical condition for the occurrence of collision- coalescence process is that there are 50 particles with the diameter of about 120 μm per liter. The radar reflectivity Z at this condition is Z = 0.149 mm^6 m^{-3} (−8.26 dBZ) from Eq. (2.3). This condition is universal regardless of the type of convective clouds. The differences in precipitation characteristics of various convective clouds depend on when and at what altitude this development process is realized. Sauvageot and Omar (1987) shows that the boundary between precipitation clouds (> 200 μm) and non-precipitation clouds is Z = 0.032 mm^6 m^{-3} (−15 dBZ) as a result of aircraft observations on the plateau (altitude 600 m) in southwestern France. Furthermore, Misumi et al. (2018b) defines drizzling clouds as

the particle with the diameter of 50 μm in 1 cm^{-3} in the observation of cloud particles at the Tokyo Skytree (at an altitude of 458 m). This definition corresponds to Z = 0.0156 mm^6 m^{-3} (−18.1 dBZ). Although the thresholds of these studies are different, there is the common feature that precipitation clouds and non-precipitation clouds are separated by radar reflectivity. In other words, although the threshold for MaxVARa(0 dBZ) is also different from theirs, there is a physical basis for setting a threshold of VARa for whether MCEs become MPEs or not. Shiino (1986) also shows that the time difference between the formation of clouds and the appearance of the bimodal particle size distribution is 18 minutes. Considering that the Ka-band radars cannot observe echoes in the stage of cloud formation, the threshold for Δt (9 minutes) is reasonable. Therefore, the indicator of MCE development reflects the characteristics of limited cumulonimbus clouds generated by the convergence of sea breeze around Tokyo, but it can be applied regardless of the type of convective cloud and the area of occurrence.

6.2. Limitation of the proposed forecast model

First, this indicator is only applicable to convective echoes formed near Ka-band radar sites because the minimum detectable reflectivity decreases with the distance from radar sites due to attenuation. Because the observation area of Ka-band radars is

narrow compared to that of centimeter-wavelength radars, a network of many Ka-band radars is required. A wide observation area also makes it possible to apply this model to fast-moving echoes. Second, the target of this model is limited to isolated cumulonimbus clouds with no other developed clouds between them and the radar site. For convective echoes accompanied by large precipitation systems such as squall lines, typhoon rainbands, or cold fronts, strong rain attenuation would affect the VAR value. In such cases, accurate observation of the VAR for weak echoes would be difficult. Similar to the limitation described above, this can also be mitigated to some extent by deploying more Ka-band radars. Third, it is difficult to forecast the rainfall amount quantitatively caused by MPE whose development is predicted by this indicator. MaxVARa (Δt= 9 minutes) of the developed MCEs and the maximum VIL of the MPEs (maximum in the MPE area) are shown in Fig. 15. The expressions for the traditional method and for the K_{dp} method are shown in Eq. (6.1) in which the coefficients for the equation are from Maki et al. (2005).

$$VIL = \begin{cases} \int_0^h 0.00393\, Z^{0.550} dh & K_{dp} \leq 0.3°\mathrm{km}^{-1} \\ & or\ 10\log Z \leq 35\mathrm{dBZ} \\ \int_0^h 0.991\, {K_{dp}}^{0.713} dh & otherwise \end{cases} \quad (6.1)$$

Here, h indicates the vertical range over which VIL is calculated and set to 10 km.

The reason why VIL is used here instead of ground rainfall amount is that MCEs and MPEs are defined by VARa, and VARa includes vertical information on total water, which does not necessarily correspond to ground rainfall. On the other hand, VIL is a similar parameter to VARa and is also an indicator of the growth of cumulonimbus clouds, so if MCEs with high VARa grow into MPEs, VIL should also be high. However, it is not shown in this figure. The correlation coefficient between these variables was almost zero (−0.0987). In addition, there were only four MPEs whose VIL exceeds 25 kg m^{-2}, which is the threshold for the precipitation system with hail observation (Ceperuelo et al. 2006). Therefore, MCEs predicted to grow to MPEs by this indicator have the potential for rainfall, but they do not always cause localized heavy rainfall. This is because the main target of this study is isolated cumulonimbus clouds, whereas hailstorms and localized heavy rainfall are often caused by organized, large-scale precipitation systems. This limitation cannot be overcome by simply increasing the number of radar sites. In order to forecast local heavy rainfall based on this indicator, it is necessary to examine the MCEs that occur around such a precipitation system.

7. Conclusions

To detect cumulonimbus clouds in their early development stages and forecast their

development, local heavy rainfall was observed by multiple Ka-band radars and operational X-band radars. The VAR was used to analyze the development of convective echoes. MCEs and MPEs were defined based on the VAR derived from Ka-band and X-band radars, respectively, and statistical analyses of the echoes and tracking information were performed. The results are summarized as follows:

1) The first detection time of MCEs was 17 minutes earlier than that of MPEs and 33 minutes earlier than the peak time of the VARa of MPEs on average.

2) There were statistically significant differences between developed and non-developed MCEs in terms of the MaxVARa, MaxAREA, ΔVARa, and ΔAREA for 6 to 12 minutes after their first detection. Among these indicators, the MaxVARa for the elapsed time Δt = 9 minutes (threshopld: 0 dBZ) would be the best indicator for practical forecasting.

3) This indicator was obtained by limited cumulonimbus clouds triggered by the convergence of sea breeze around Tokyo. However, the thresholds of MaxVARa and Δt are consistent with previous studies and have been shown to be applicable regardless of convective cloud type or region of occurrence.

4) Nowcasting model for predicting MCE development was proposed using the MaxVARa (Δt = 9 minutes) as an indicator. This model is expected to forecast

rainfall earlier than conventional X-band radars, although there are following restrictions on its use;

a. This indicator is only applicable to convective echoes formed near Ka-band radar sites because the minimum detectable reflectivity decreases with the distance from radar sites due to attenuation.
b. The target of this model is limited to isolated cumulonimbus clouds, which are relatively unaffected by precipitation attenuation.
c. It is difficult to forecast the rainfall amount quantitatively caused by MCE whose development is predicted by this indicator. Forecasted MCEs have the potential for rainfall, but they do not always cause localized heavy rainfall.

In order to forecast local heavy rainfall based on this indicator, it is necessary to examine the MCEs that occur around such a precipitation system.

Acknowledgments

The author thanks to Dr. Ryohei Misumi, Dr. Shinya Shimokawa, and Dr. Yukari Shusse of the adviser of this study for productive discussions and encouragements, Dr. Namiko Sakurai, Dr. Kohin Hirano, Dr. Koyuru Iwanami, Dr. Shin-ichi Suzuki, Dr. Ryohei Kato, and Dr. Tadayasu Ohigashi of NIED (National Research Institute for Earth Science and Disaster Resilience) for many advices, and Prof. Michiaki Sugita, Prof. Jun Asanuma, Prof. Maki Tsujimura, and Prof. Tsutomu Yamanaka of Tsukuba University hydrological science for the meaningful suggestion at presentations. He expresses special thanks to Dr. Takeshi Maesaka and Dr. Shingo Shimizu for many assistance for radar data analysis and AITCC. The Ministry of Land, Infrastructure, Transport and Tourism XRAIN data were collected and provided under the Data Integration and Analysis System (DIAS) developed and operated by the Ministry of Education, Culture, Sports, Science and Technology.

References

Borque, P., P. Kollias, and S. Giangrande, 2014: First observations of tracking clouds using scanning ARM cloud radars, *J. Appl. Meteor. Climatol.*, **53**, 2732-2746, doi: 10.1175/JAMC-D-13-0182.1.

Ceperuelo, M, M. C. Llasat, and T. Rigo, 2006: Rainfall events and hailstorms analysis program (RHAP), *Adv. Geosci.*, **7**, 205-213, doi: 10.5194/adgeo-7-205-2006.

Chandrasekar, V., H. Fukatsu, and K. Mubarak, 2003: Global mapping of atten uation at Ku- and Ka-band, *IEEE Trans. Geosci. Remote Sens.* **41**, 2166-2176, doi: 10.1109/TGRS.2003.815973.

Cressman P.G., 1959: An operational objective analysis system, *Mon. Wea. Rev.*, **87**, 367-374.

Fujibe, F., K. Sakagami, K. Chubachi, and K. Yamashita, 2002: Surface wind patterns preceding short-time heavy rainfall in Tokyo in the afternoon of midsummer days, *Tenki,* **49**, 31-41 (in Japanese with English abstract).

Fukao, S., and K. Hamazu, 2009: Radar remote sensing of weather and atmosphere, *Kyoto University Press*, 502p (in Japanese).

Hamazu, K., H. Hashiguchi, T. Wakayama, T. Matsuda, R. J. Doviak, and S. Fukao, 2003: A 35-GHz scanning Doppler radar for fog observations, *J. Atmos. Oceanic*

Technol., **20**, 972-986, doi: 10.1175/1520-0426(2003)20<972:AGSDRF>2.0.CO;2.

Hirano, K., and M. Maki, 2010: Method of VIL calculation for X-band polarimetric radar and potential of VIL for nowcasting of localized severe rainfall -Case study of the Zoshigaya downpour, 5 August 2008-, *SOLA*, **6**, 89–92, doi: 10.2151/sola.2010-023.

Hirano, K., and M. Maki, 2018: Imminent nowcasting for severe rainfall using vertically integrated liquid water content derived from X-band polarimetric radar, *J. Meteor. Soc. Japan,* **96**, 201-220, doi: 10.2151/jmsj.2018-028.

Ishihara, M., 2012: Radar echo population of thunderstorms generated on the 2008 Zoshigaya-rainstorm day and nowcasting of thunderstorm-induced local heavy rainfalls. Part I: Three-dimensional radar echo population of the thunderstorms, *Tenki,* **59**, 27-39 (in Japanese with English abstract).

Kato, A., and M. Maki, 2009: Localized heavy rainfall near Zoshigaya, Tokyo, Japan on 5 August 2008 observed by X-band polarimetirc radar: Preliminary analysis, *SOLA*, **5**, 89-92, doi:10.2151/sola.2009–023.

Kato, R., S. Shimizu, K. Shimone, and K. Iwanami, 2017: Very short time range forecasting using CReSS-3DVAR for a meso-γ-scale, localized extremely heavy rainfall event: Comparison with an extrapolation-based nowcast, *J. Disaster Res.,* **12**,

967-979, doi: 10.20965/jdr.2017.p0967.

Kato, T, 2020: Quasi-stationary band-shaped precipitation systems, named “Senjo-Kousuitai”, causing localized heavy rainfall in Japan, *J. Meteor. Soc. Japan*, **98**, 485-509, doi:10.2151/jmsj.2020-029.

Khain, A., M. Pinsky, L. Magaritz, O. Krasnov, and H. W. J. Russchenberg, 2008: Combined observational and model investigations of the Z-LWC relationship in stratocumulus clouds, *J. Appl. Meteor. Climatol*., **47**, 591-606, doi: 10.1175/2007JAMC1701.1.

Kigawa, S., 2014a: Techniques of precipitation analysis and prediction nowcasts, available online at https://www.jma.go.jp/jma/en/Activities/Techniques_of_Precipitation_Analysis_and_Prediction_developed_for_HRPNs.pdf [accessed 27 January 2021].

Kigawa, S., 2014b: Techniques of precipitation analysis and prediction nowcasts, *Weather service bulletin*, **81**, 55-76 (in Japanese).

Kim, D.-S., M. Maki, S. Shimizu, and D.-I. Lee, 2012: X-band dual-polarization radar observations of precipitation core development and structure in a multicellular storm over Zoshigaya, Japan, on August 5, 2008. *J. Meteor. Soc. Japan*, **90**, 701–719, doi: 10.2151/jmsj.2012-509.

Kollias, P., N. Bharadwaj, K. Widener, I. Jo, and K. Johnson, 2014: Scanning ARM cloud radars. Part I: operational sampling strategies, *J. Atmos. Oceanic Technol.*, **31**, 569-582, doi: 10.1175/JTECH-D-13-00044.1.

Liebe, H. J., 1985: An updated model for millimeter wave propagation in moist air, *Radio Sci.,* **20**, 1069-1089, doi: 10.1029/RS020i005p01069.

Maki, M., S.-G. Park, and V. N. Bringi, 2005: Effect of natural variations in rain drop size distributions on rain rate estimators of 3 cm wavelength polarimetric radar, *J. Meteor. Soc. Japan*, **83**, 871−893, doi: 10.2151/jmsj.83.871.

Maesaka, T., M. Maki, K. Iwanami, S. Tsuchiya, K. Kieda, and A. Hoshi, 2011: Operational rainfall estimation by X-band MP radar network in MLIT, Japan, *Proceedings of 35th Conference on Radar Meteorology*, Pittsburgh, P11.142.

Maesaka, T., K. Iwanami, S. Suzuki, Y. Shusse, and N. Sakurai, 2015: Cloud radar network in Tokyo metropolitan area for early detection of cumulonimbus generation, *Proceedings of 37th Conference on Radar Meteorology*, Norman, 174.

Maesaka, T., 2018: Cloud radars, *Remote Sensing of Clouds and Precipitation*, C. Andronache, Ed., Springer-Verlag, 137-152.

Marrocu, M., and L. Massidda, 2020: Performance comparison between deep learning and optical flow-based techniques for nowcast precipitation from radar images,

MDPI, **2**, 194-210, doi: 10.3390/forecast2020011.

Matrosov, S. Y., 2005: Attenuation-based estimates of rainfall rates aloft with vertically pointing Ka-band radars, *J. Atmos. Oceanic Technol,* **22**, 43-54, doi: 10.1175/JTECH-1677.1.

Ministry of Land, Infrastructure, Transport and Tourism, 2011: Disaster report of Typhoon 1112(TALAS) (in Japanese), available online at http://www.mlit.go.jp/saigai/saigai_110901.html [accessed 27 January 2021].

Ministry of Land, Infrastructure, Transport and Tourism, 2020: Disaster report of heavy rainfall in July 2020 (in Japanese), available online at http://www.mlit.go.jp/saigai/saigai_200704.html [accessed 27 January 2021].

Misumi, R., N. Sakurai, T. Maesaka, S. Suzuki, S. Shimizu, and K. Iwanami, 2018a: Transition process from non-precipitating cumuli to precipitating convective clouds over mountains: obsevation by Ka-band Doppler radar and stereo photogrammetry, *J. Meteor. Soc. Japan*, **96A**, 51-66, doi: 10.2151/jmsj.2017-021.

Misumi, R., Y. Uji, Y. Tobo, K. Miura, J. Uetake, Y. Iwamoto, T. Maesaka, and K. Iwanami, 2018b: Characteristics of droplet size distribution in low-level stratiform clouds observed from Tokyo Skytree, *J. Meteor. Soc. Japan*, **96**, 405-413, doi: 10.2151/jmsj.2018-040.

Nakakita, E., R. Nishiwaki, H. Yamabe, and K. Yamaguchi, 2013: Research on the prognostic risk of baby cell for guerilla-heavy rainfall considering by vorticity with Doppler velocity, *J. JSCE*, Ser. B1, **69**, I_325-I_330 (in Japanese with English abstract).

Nakakita, E., H. Sato, and K. Yamaguchi, 2016: Fundamental analysis of vortex tubes inside the baby cells of guerilla-heavy rainfall, *J. JSCE*, Ser. B1, **72**, I_199-I_204 (in Japanese with English abstract).

Nakakita, E., T. Niibo, H. Sato, K. Yamaguchi, T. Ohigashi, T. Shinoda, and K. Tsuboki, 2017: Preliminary analysis of cumulonimbus cloud structure using multi parameter information of Ka-band polarimetric Dopper radar, *DPRI Annuals*, **60B**, 559-575 (in Japanese with English abstract).

Nishikawa, M., K. Nakamura, Y. Fujiyoshi, K. Nakagawa, H. Hanado, H. Minda, S. Nakai, T. Kumakura, and R. Oki, 2016: Radar attenuation and reflectivity measurements of snow with dual Ka-band radar, *IEEE Trans. Geosci. Remote Sens.* **54**, 714-722, doi: 10.1109/TGRS.2015.2464099.

Nishiwaki, N., R. Misumi, S. Shimizu, T. Maesaka, K. Iwanami, N. Sakurai, M. Maki, S. Suzuki, A. Kato, and A. Yamaji, 2013: Behavior and structure of convective clouds developing around a mountainous area observed by stereo photogrammetry and Ka-

band and X-band radars: Case study of norther Kanto, Japan, *J. Meteor. Soc. Japan*, **91**, 609-626, doi: 10.2151/jmsj.2013-504.

Oh, S.-B., Y. H. Lee, J.-H. Jeong, Y.-H. Kim, and S. Joo, 2018: Estimation of the liquid water content and Z-LWC relationship using Ka-band cloud radar and a microwave radiometer, *Meteorol. Appl.*, **25**, 423-434, doi: 10.1002/met.1710.

Otsuka, S., G. Tuerhong, R. Kikuchi, Y. Kitano, Y. Taniguchi, J. J. Ruiz, S. Satoh, T. Ushio, and T. Miyoshi, 2016: Precipitation nowcasting with three-dimensional space-time extrapolation of dense and frequent phased-array weather radar observations, *Wea. Forecasting*, **31**, 329-340, doi: 10.1175/WAF-D-15-0063.1.

Park, S.-G., V. N. Bringi, V. Chandrasekar, M. Maki and K. Iwanami, 2005: Correction of radar reflectivity and differential reflectivity for rain attenuation at X band. Part1: Theoretical and empirical basis, *J. Atmos. Oceanic Technol,* **22**, 1621-1632, doi: 10.1175/JTECH1803.1.

Radhakrishnan, C., and V. Chandrasekar, 2020: CASA prediction system over Dallas-Fort Worth urban network: Blending of nowcasting and high-resolution numerical weather prediction model, *J. Atmos. Oceanic Technol,* **37**, 211-228, doi: 10.1175/JTECH-D-18-0192.1.

Ruzanski, E., V. Chandrasekar, and Y. Wang, 2010: The CASA nowcasting system, *J.*

Atmos. Oceanic Technol, **28**, 640-655, doi: 10.1175/2011JTECHA1496.1.

Saito, K., M. Kunii, and K. Araki, 2018: Cloud resolving simulation of a local heavy rainfall event on 26 August 2011 observed in TOMACS, *J. Meteor. Soc. Japan*, **96**, 175–199, doi: 10.2151/jmsj.2018-027.

Sakurai, N., K. Iwanami, T. Maesaka, S. Suzuki, S. Shimizu, R. Misumi, D.–S. Kim, and M. Maki, 2012: Case study of misoscale convective echo behavior associated with cumulonimbus development observed by Ka-band Doppler radar in the Kanto Region, Japan, *SOLA,* **8**, 107-110, doi: 10.2151/sola.2012-027.

Sauvageot, H., and J. Omar, 1986: Radar reflectivity of cumulus clouds, *J. Atmos. Oceanic Technol,* **4**, 264-272, doi: 10.1175/1520-0426(1987)004<0264:RROCC>2.0.CO;2.

Shiino, J, 1986: A study of the precipitation and dynamical behavior of maritime convective clouds, *J. Meteorol, Res.,* **37**, 115-190 (in Japanese with English abstract).

Shimizu, S., and H. Uyeda, 2012: Algorithm for the identification and tracking of convective cells based on constant and adaptive threshold methods using a new cell-merging and -splitting scheme, *J. Meteor. Soc. Japan*, **90**, 869–889, doi: 10.2151/jmsj.2012-602.

Takahashi, N., T. Ushio, K. Nakagawa, F. Mizutani, K. Iwanami, A. Yamaji, T.

Kawagoe, M. Osada, T. Ohta, and M. Kawasaki, 2019: Development of multi-parameter phased array radar (MP-PAWR) and early detection of torrential rainfall and tornado risk, *J. Disaster Res.*, **14**, 235-247, doi: 10.20965/jdr.2019.p0235.

Uematsu, A., H. Hashiguchi, M. Teshiba, H. Tanaka, K. Hirashima, and S. Fukao, 2005: Moving cellular structure of fog echoes obtained with a millimeter-wave scanning Doppler radar at Kushiro, Japan, *J. Appl. Meteor.*, **44**, 1260-1273, doi: 10.1175/JAM2274.1.

Ushio, T., T. Wu, and S. Yoshida, 2015: Review of recent progress in lightning and thunderstorm detection techniques in Asia, *Atmos. Res.*, **154**, 89–102, doi: 10.1016/j.atmosres.2014.10.001.

Yoshikawa, E., T. Ushio, Z. Kawasaki, S. Yoshida, T. Morimoto, F. Mizutani, and M. Wada, 2013: MMSE beam forming on fast-scanning phased array weather radar, *IEEE Trans. Geosci. Remote Sens.*, **51**, 3077–3088, doi: 10.1109/TGRS.2012.2211607.

Yoshida, S., R. Misumi, S. Shimizu, T. Maesaka, K. Iwanami, and M. Maki, 2012: Validation of short-term forecasting of meso-γ-scale convective systems based on a cell-tracking system, *SOLA*, **8**, 141-144, doi: 10.2151/sola.2012-035.

Yoshida, S., T. Ushio, S. Yoshida, S. Shimamura, K. Maruo, and N. Takada, 2013: The structure of convective systems observed by Phased array radar in the Kinki region,

Japan, *Proceedings of 36th Conference on Radar Meteorology*, Breckenridge, 139.

Wilson, J. W., N. A. Crook, K. Mueller, J. Sun, and M. Dixon, 1998: Nowcasting thunderstorms: A status report, *Bull. Am. Meteorol. Soc. (BAMS)*, **79**, 2079-2100, doi: 10.1175/1520-0477(1998)079<2079:NTASR>2.0.CO;2.

Table 1. Specifications of Ka-band radars.

	TKB	OTA	HNO	NTK	MTD
Frequency	34.84 GHz	34.86 GHz	34.88 GHz	34.91 GHz	34.93 GHz
Beam width	0.31°				
Pulse width	1.0 μs (short) / 55 μs (long)				
PRF	Dual, 1980 Hz / 1584 Hz				
Noise level	− 110 dBm (short) − 126 dBm (long)	− 113 dBm (short) − 125 dBm (long)	− 112 dBm (short) − 126 dBm (long)	− 114 dBm (short) − 128 dBm (long)	− 110 dBm (short) − 123 dBm (long)
Range interval	150 m				
Products	$Z, V, W, Z_{DR}, K_{dp}, \rho_{hv}$			Z, V, W	

Table 2. Specifications of X-band radars.

	SAI	SYK	FNB	YAT	UJI
Frequency	9.76 GHz	9.78 GHz	9.72 GHz	9.74 GHz	9.78 GHz
Beam width	1.04° (H) 1.06° (V)	1.05° (H, V)	1.07° (H) 1.04°(V)	1.03° (H, V)	1.03° (H, V)
Pulse width	1.0 μs (short) 48.0μs (long)	1.0 μs	1.0 μs (short) 32.0 μs (long)	1.0 μs (short) 32.0 μs (long)	1.0 μs (short) 32.0 μs (long)
PRF	SYK : Dual, 1800 Hz / 1440 Hz the others: Dual, 1980 Hz / 1584 Hz				
Noise level	− 113 dBm (short) − 107 dBm (long)	− 107 dBm	− 102 dBm (short) − 116 dBm (long)	− 102 dBm (short) − 117 dBm (long)	− 102 dBm (short) − 117 dBm (long)
Range interval	150 m				
Products	$Z, V, W, Z_{DR}, K_{dp}, \rho_{hv}$				

Table 3. Cases used for analysis.

No.	Time and date [JST]	Number of MCEs	
		Developed	Non-developed
1	1300-1700 4 Aug. 2016	6	1
2	1300-1700 9 Aug. 2017	2	7
3	1400-1700 19 Aug. 2017	2	7
4	1000-1400 30 Aug. 2017	5	24
Total number of MCEs		15	39

Table 4. Characteristics of developed MCEs. t_1 and t_2 indicate the lead time to the first detection of MPE and to the first peak time of MPE, respectively. "Initial" means the initial values of MCEs, and "Max" and "Δ" mean the maximum values and increase amounts, respectively, in the period between the first detection of MCEs and MPEs.

MCE No.	Case No.	t_1 [min]	t_2 [min]	VARa			MCE area		
				Initial [dBZ]	Max [dBZ]	Δ [dB]	Initial [km²]	Max [km²]	Δ [km²]
1	1	12	32	−13.5	5.7	19.2	4.6	18.2	13.5
2	1	12	32	−3.4	5.2	8.6	3.6	21.0	17.4
3	1	8	28	−6.6	4.8	11.4	4.8	21.6	16.8
4	1	10	25	−5.9	8.5	14.4	6.2	12.7	6.5
5	1	17	17	−14.8	19.7	34.5	4.0	24.7	20.6
6	1	6	16	−13.6	3.1	16.7	4.6	8.4	3.7
7	2	16	36	−13.4	1.1	14.5	4.7	24.6	19.9
8	2	13	43	−7.4	8.7	16.1	6.1	31.3	25.2
9	3	11	41	−7.7	8.8	16.5	13.5	35.5	21.9
10	3	24	29	−10.4	20.6	31.0	4.5	41.2	36.7
11	4	33	53	−15.9	8.0	23.9	5.5	73.4	67.9
12	4	8	28	−14.1	2.5	16.6	9.5	42.4	32.9
13	4	14	24	−11.7	13.7	25.4	10.5	41.5	31.0
14	4	50	65	−4.6	8.5	13.1	4.6	52.6	48.0
15	4	16	21	−16.0	10.7	26.7	5.9	55.4	49.5
Mean value		16.7	32.7	−8.6	12.9	19.2	6.2	33.6	27.4

Table 5. Results of the Lepage test. Δt indicates the elapsed time since the first detection of MCEs. When a value exceeds 9.21, the difference is significant at the 99 % confidence level.

Indicator	Δt				
	3min	6min	9min	12min	15min
MaxVARa	9.62	18.77	26.20	22.42	18.25
ΔVARa	5.78	15.44	18.97	16.13	14.36
MaxAREA	16.77	18.00	17.16	13.47	7.01
ΔAREA	17.27	17.27	17.82	15.12	7.98

Table 6. Maximum threat scores obtained using various indicators.

Indicator	Δt				
	3min	6min	9min	12min	15min
MaxVARa	40.9 %	57.1 %	83.3 %	90.0 %	85.7 %
ΔVARa	37.8 %	52.2 %	66.7 %	70.0 %	66.7 %
MaxAREA	52.6 %	55.0 %	64.7 %	71.4 %	55.6 %
ΔAREA	58.8 %	56.3 %	62.5 %	76.9 %	60.0 %

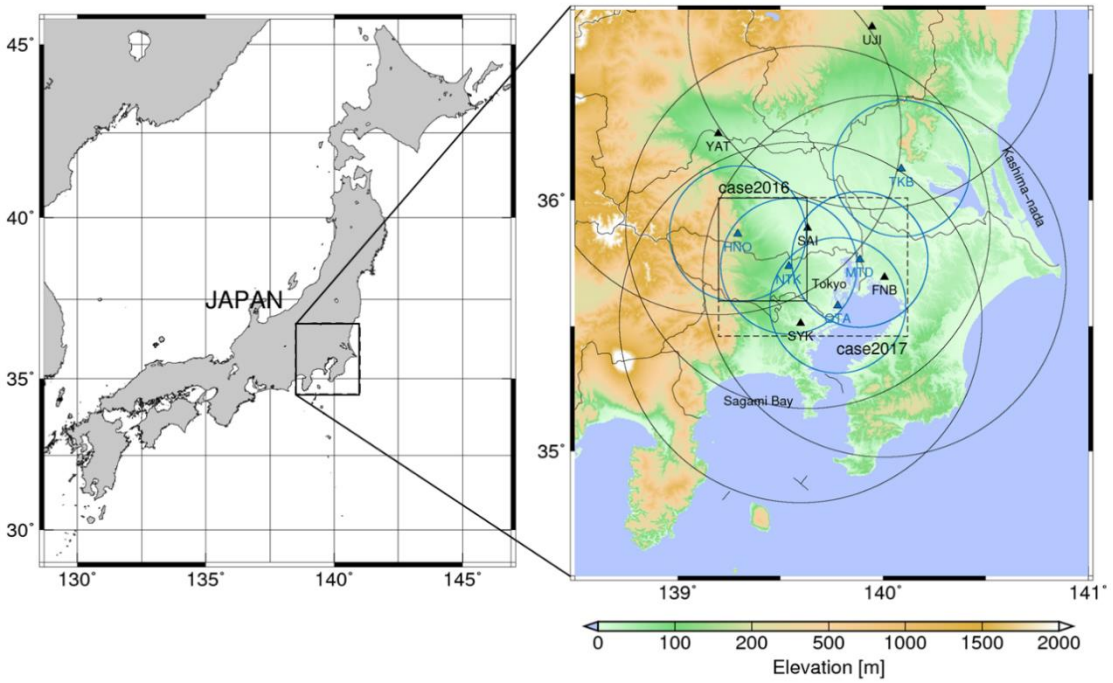

Fig. 1. Locations of radar sites and study areas. Blue triangles and circles represent Ka-band radar sites and observation ranges, respectively. Black triangles and circles represent X-band radar sites and observation ranges, respectively. Black solid and dashed frames in the right figure are the study areas in 2016 and 2017, respectively.

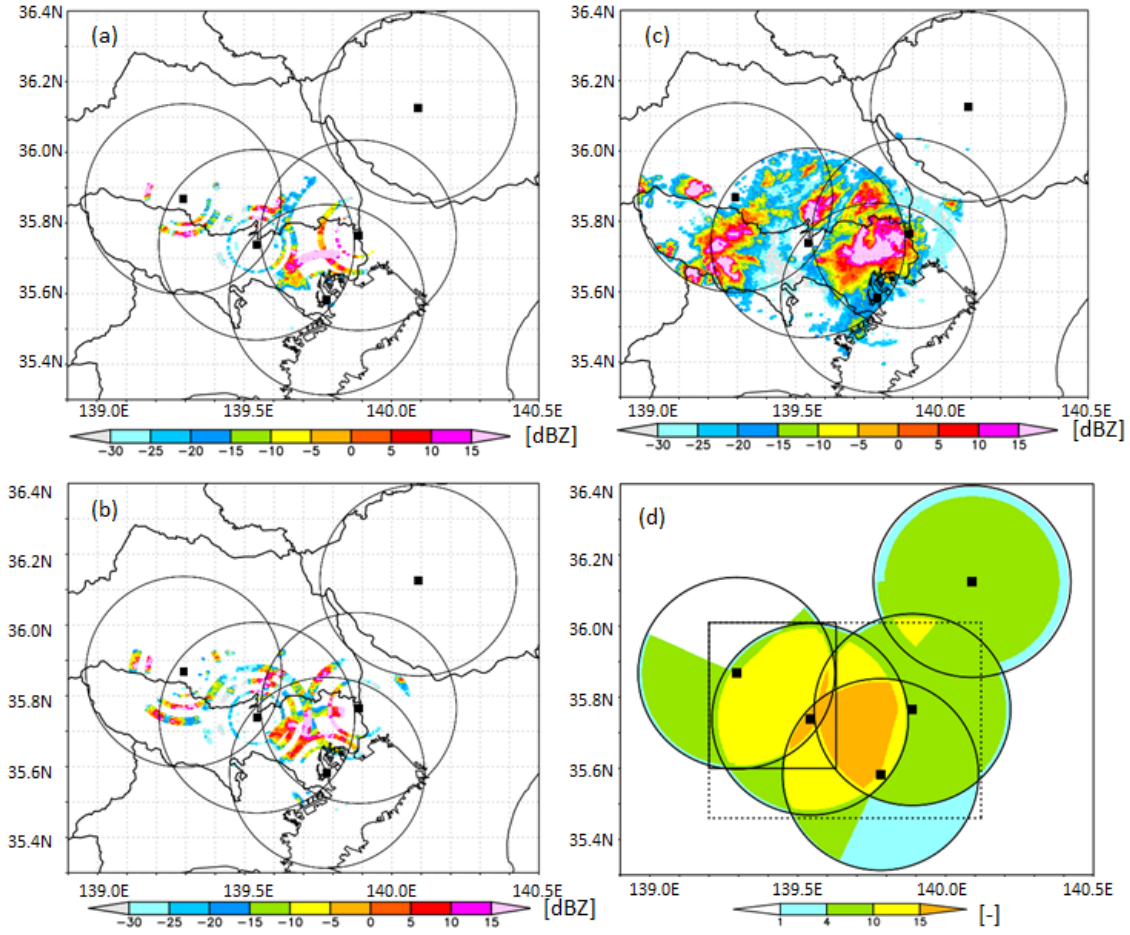

Fig. 2. Reflectivity of Ka-band radars at altitudes of (a) 3000 m and (b) 4000 m. (c) VAR and (d) the number of PPIs that contribute to VAR. Circles indicate the observation range of Ka-band radars, whose locations are denoted by black squares. Black solid and dashed frames in (d) are the study areas in 2016 and 2017, respectively (see Fig. 1).

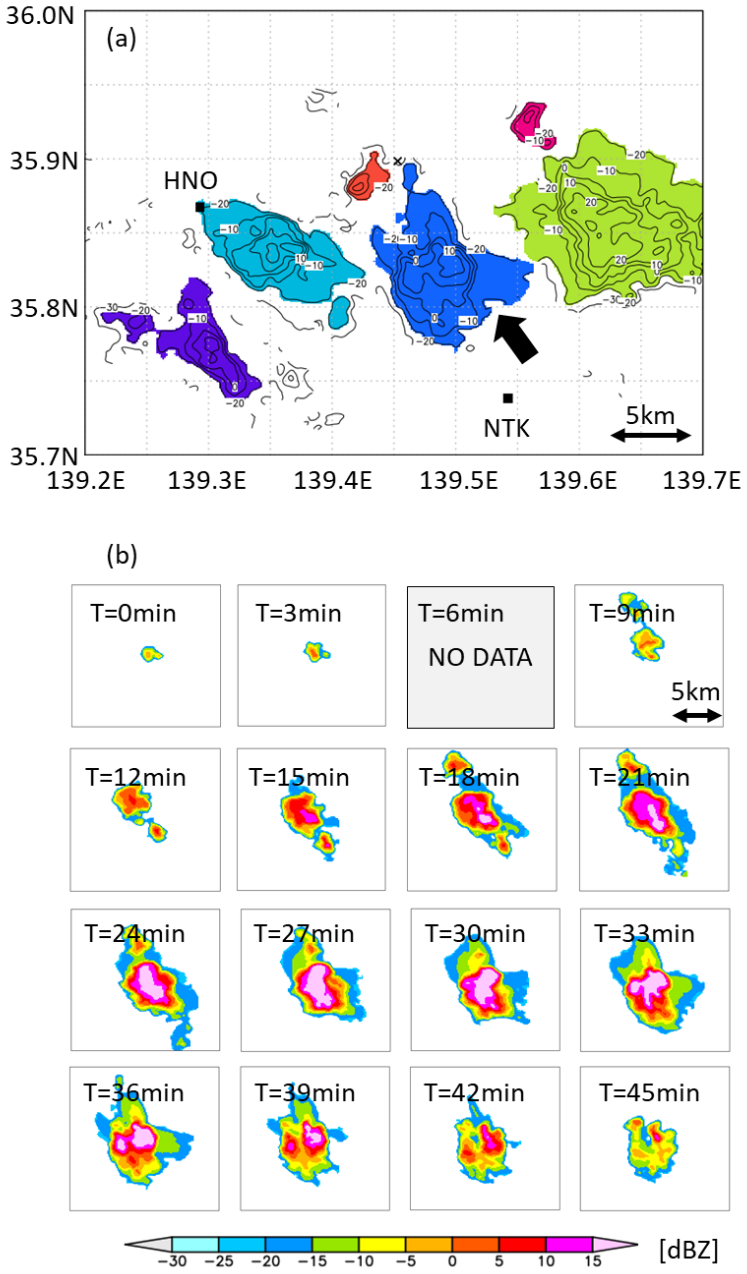

Fig. 3. (a) Examples of MCE detection and tracking. Colored areas correspond to detected MCEs. Contour lines for VAR are drawn every 10 dBZ. Black squares indicate HNO and NTK sites. (b) Time series of VAR for MCE indicated by black arrow in (a).

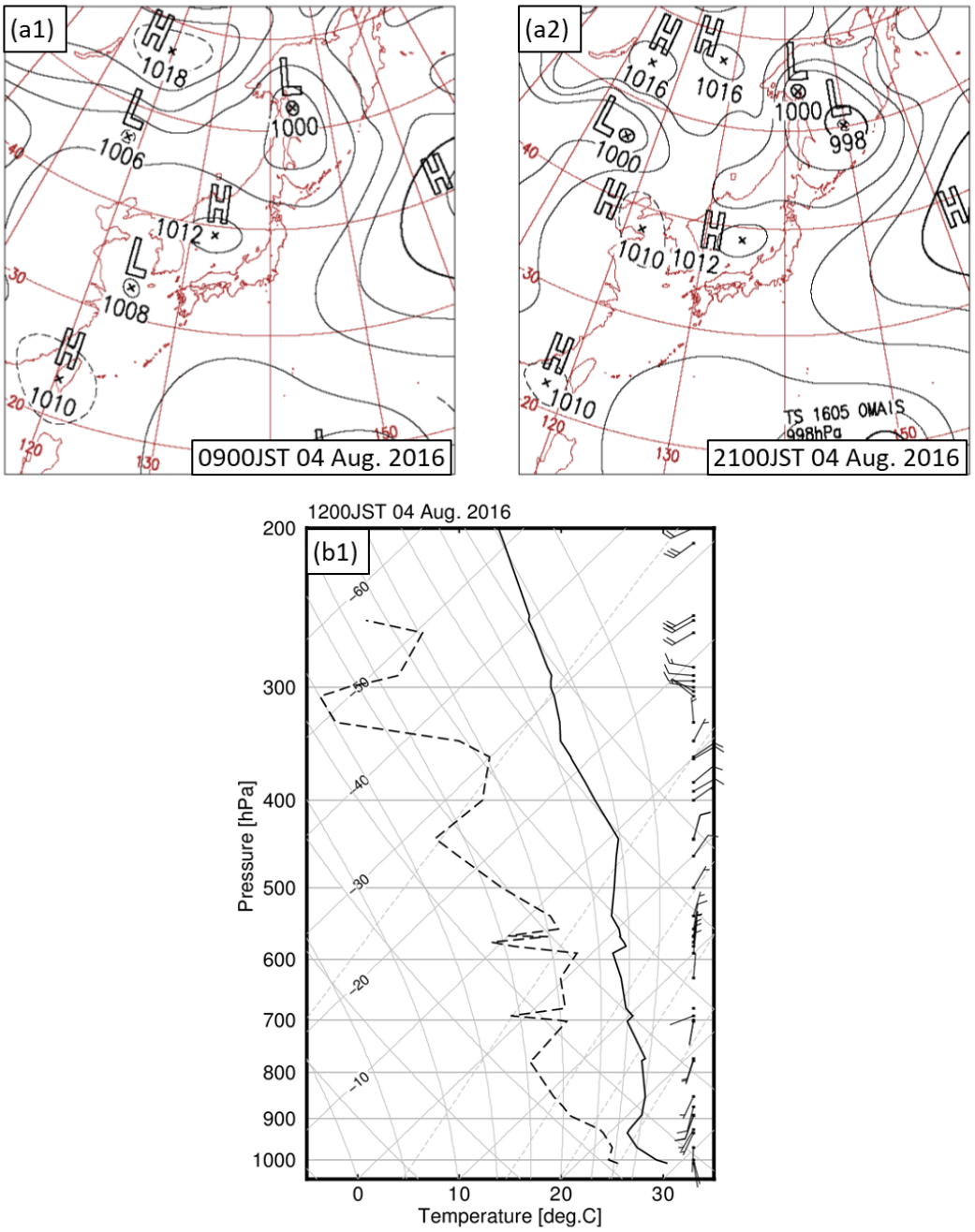

Fig. 4. (a) Surface weather maps at 0900 JST (a1) and 2100 JST (a2) on 4 August 2016. (b) Observed sounding from Tateno plotted on a standard skew $\mathrm{T} - \log p$ diagram, for 1200 JST.

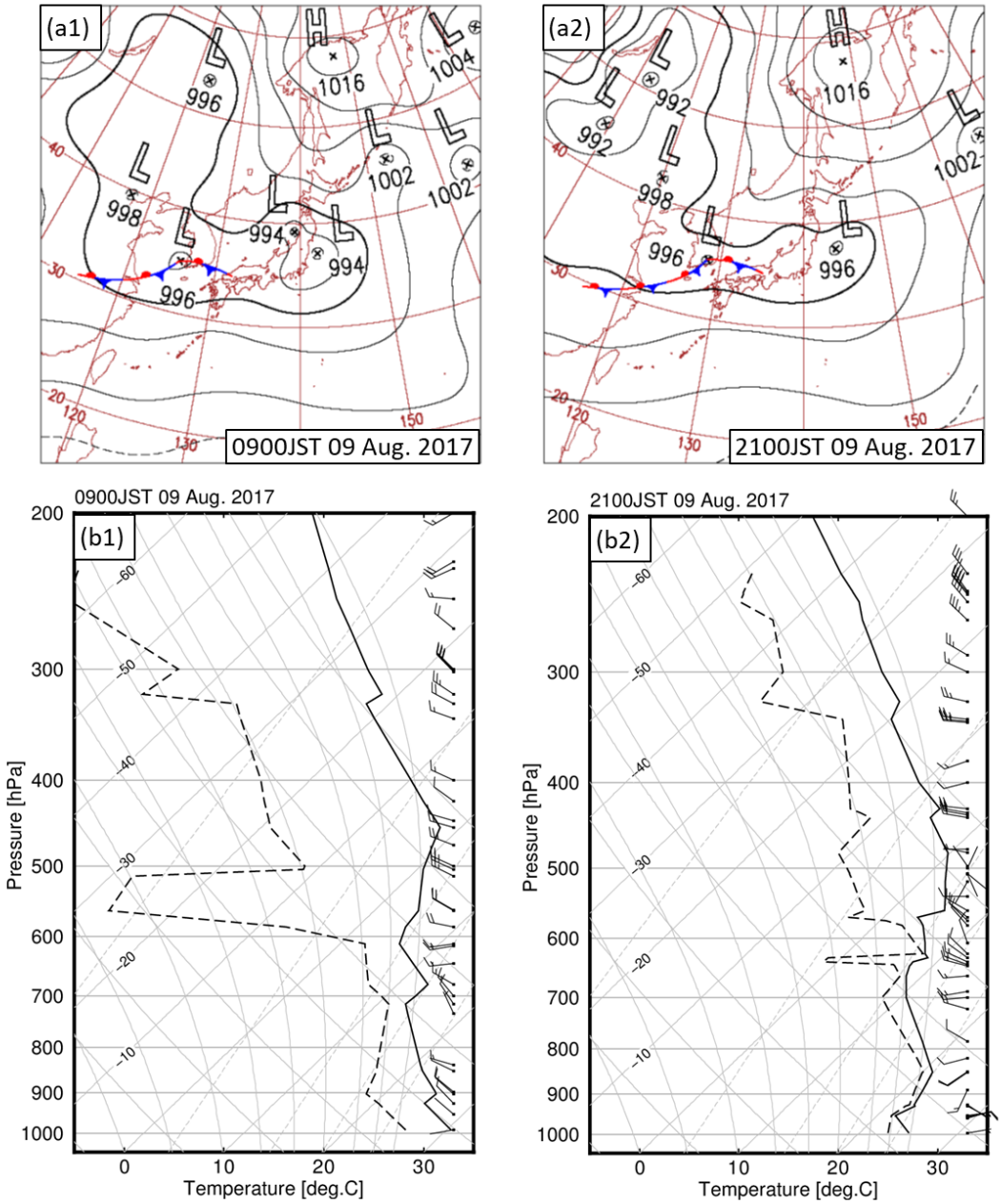

Fig. 5. Surface weather maps and observed soundings from Tateno at 0900 JST (a1, b1) and 2100 JST (a2, b2) on 9 August 2017.

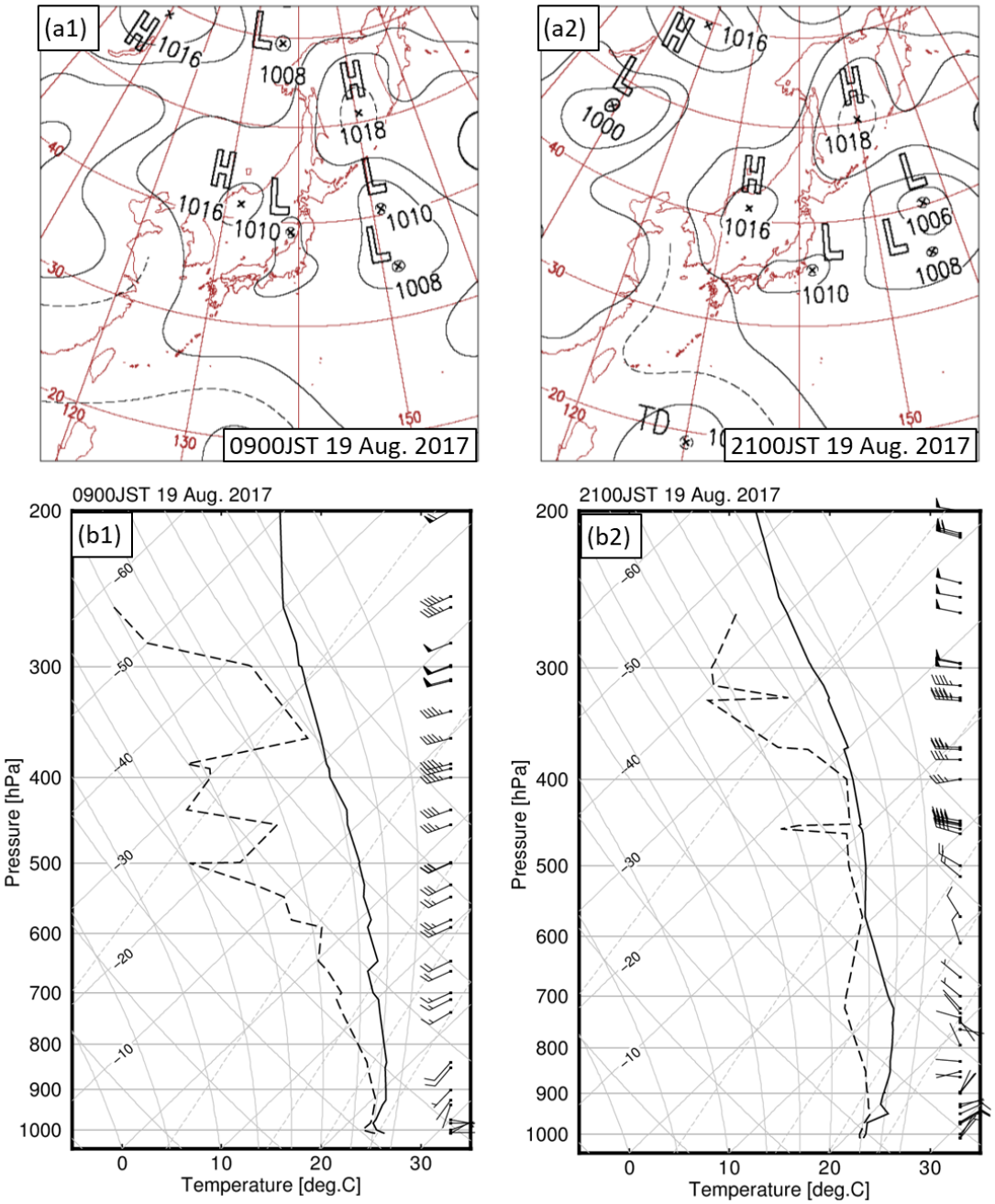

Fig. 6. Surface weather maps and observed soundings from Tateno at 0900 JST (a1, b1) and 2100 JST (a2, b2) on 19 August 2017.

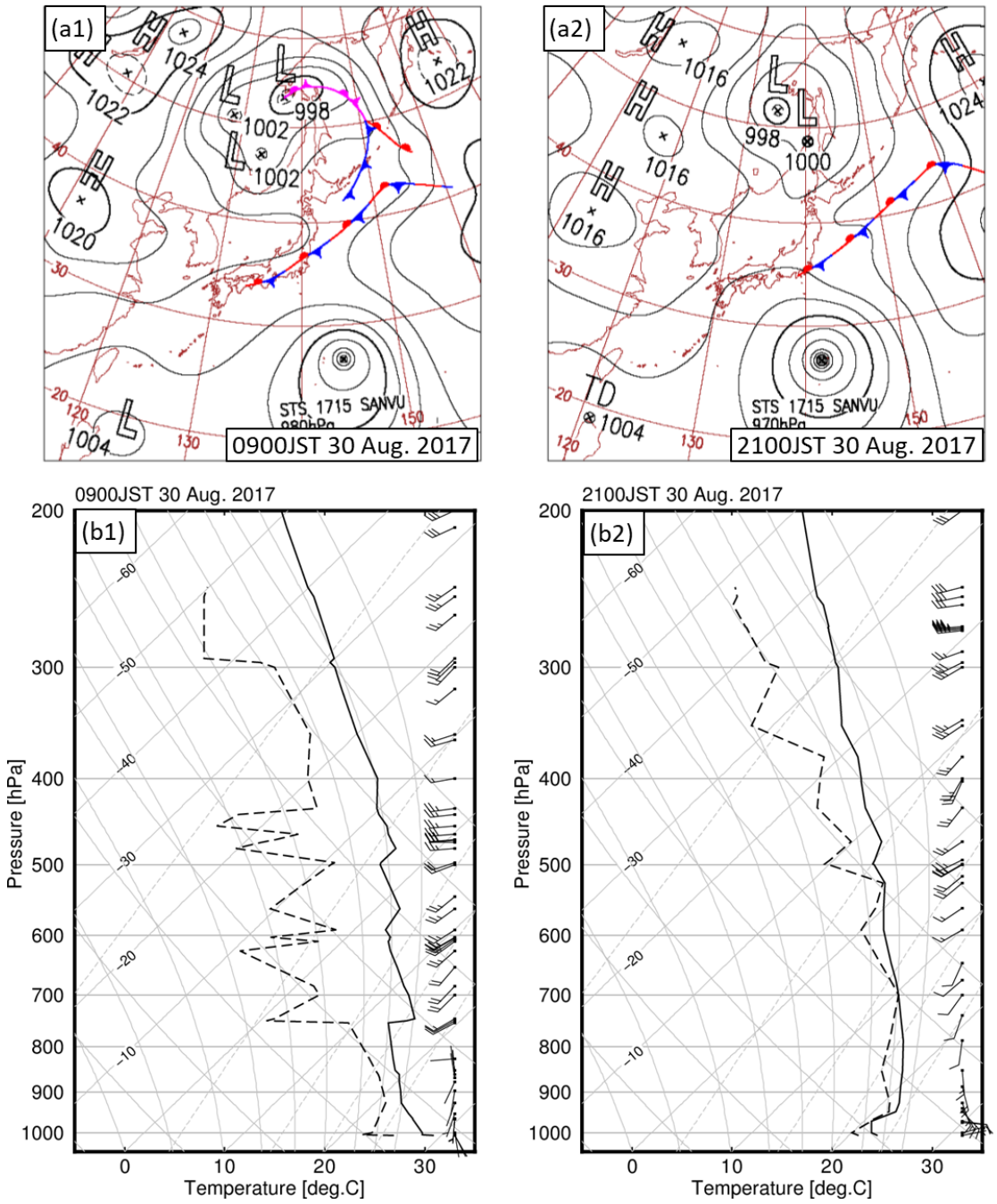

Fig. 7. Surface weather maps and observed soundings from Tateno at 0900 JST (a1, b1) and 2100 JST (a2, b2) on 30 August 2017.

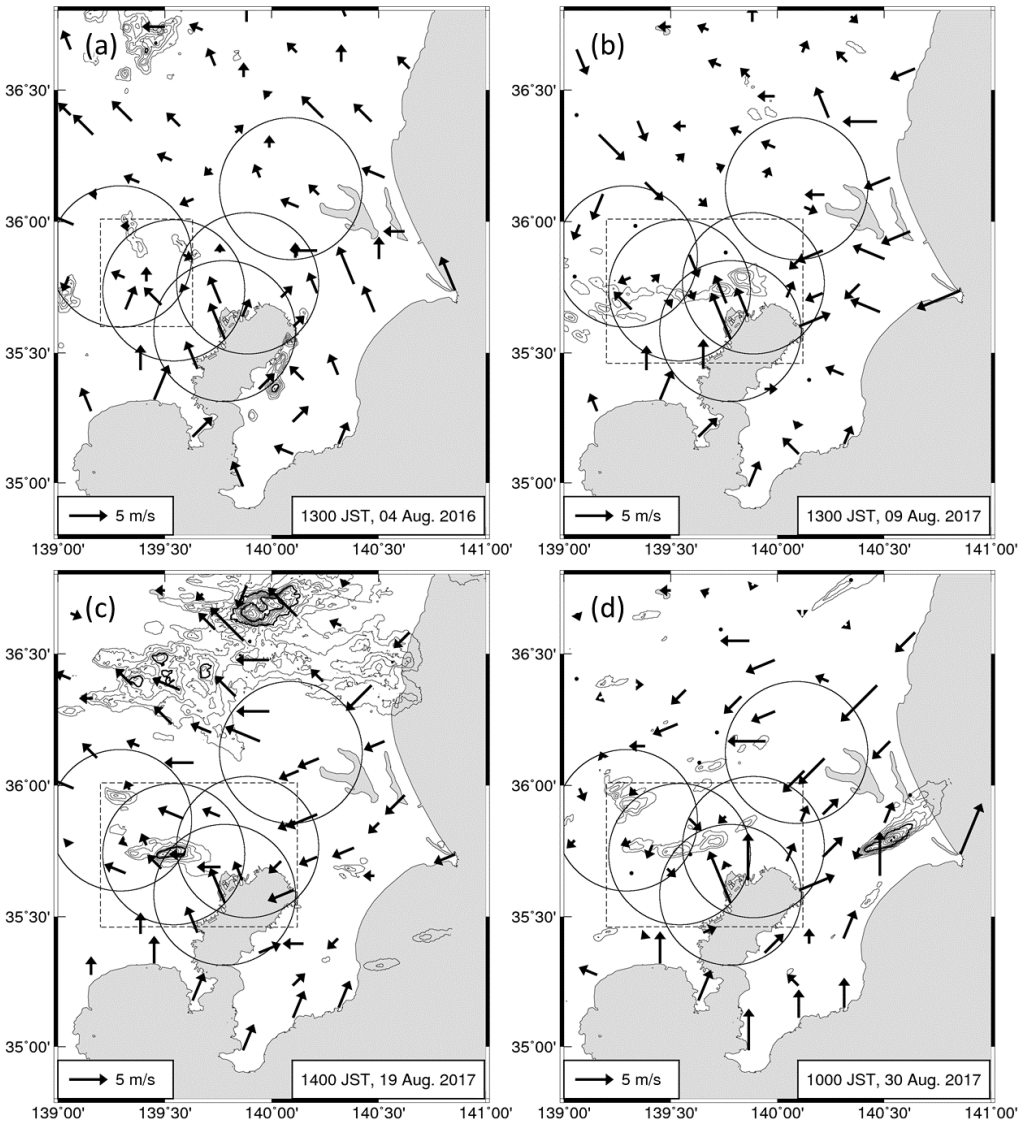

Fig. 8. Surface wind observed at the Automated Meteorological Data Acquisition System (AMeDAS; arrows) and total rainfall amount observed by XRAIN (contours) in the case studies. Winds were observed at (a) 1300 JST on 4 August 2016, (b) 1300 JST on 9 August 2017, (c) 1400 JST on 19 August 2017, and (d) 1000 JST on 30 August 2017. Contours are drawn every 10 mm and thick lines indicate 50 mm.

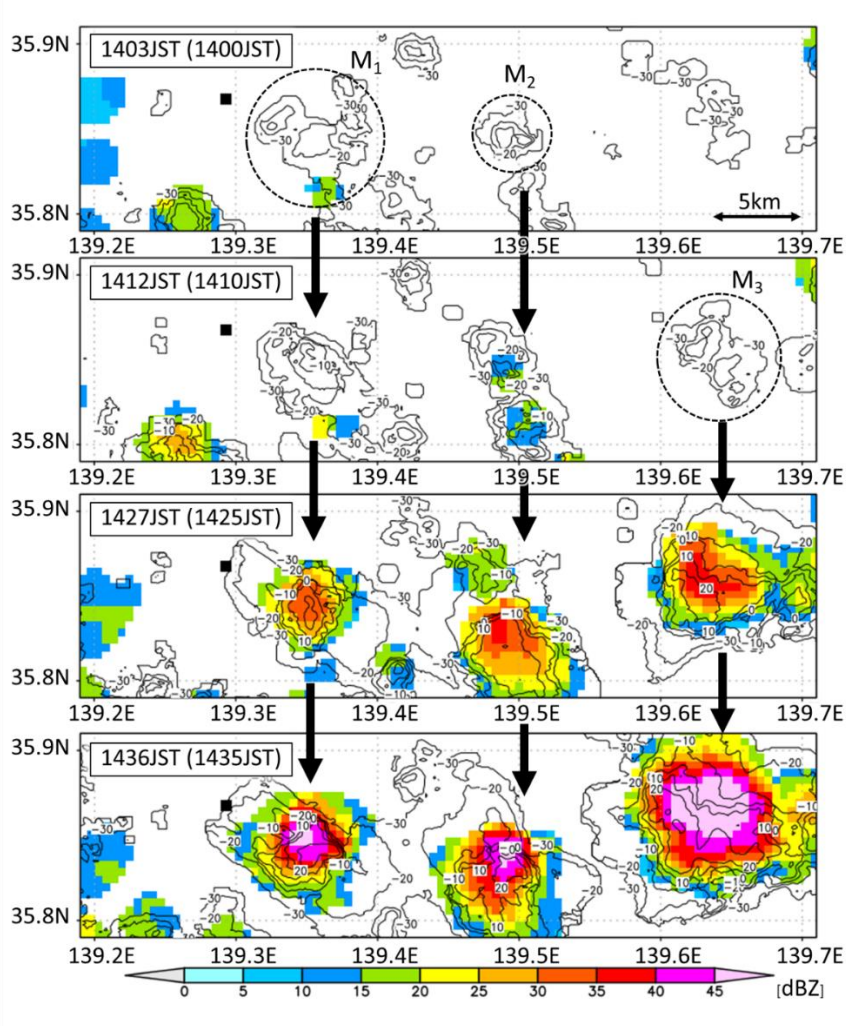

Fig. 9. VAR for developing MCEs and MPEs on 4 August, 2016 (CASE1). Contours and shaded grid represent VAR for Ka-band and X-band radars, respectively. Time in the figure is for Ka-band radar measurements. Time in parentheses is for X-band radar measurements. Black square indicates HNO radar site. Broken-line circles represent first MCEs. The average height of CAPPI data contributing to each VAR of Ka-band radars was 2.7 km at 1403 JST and 3.8 km at 1436 JST.

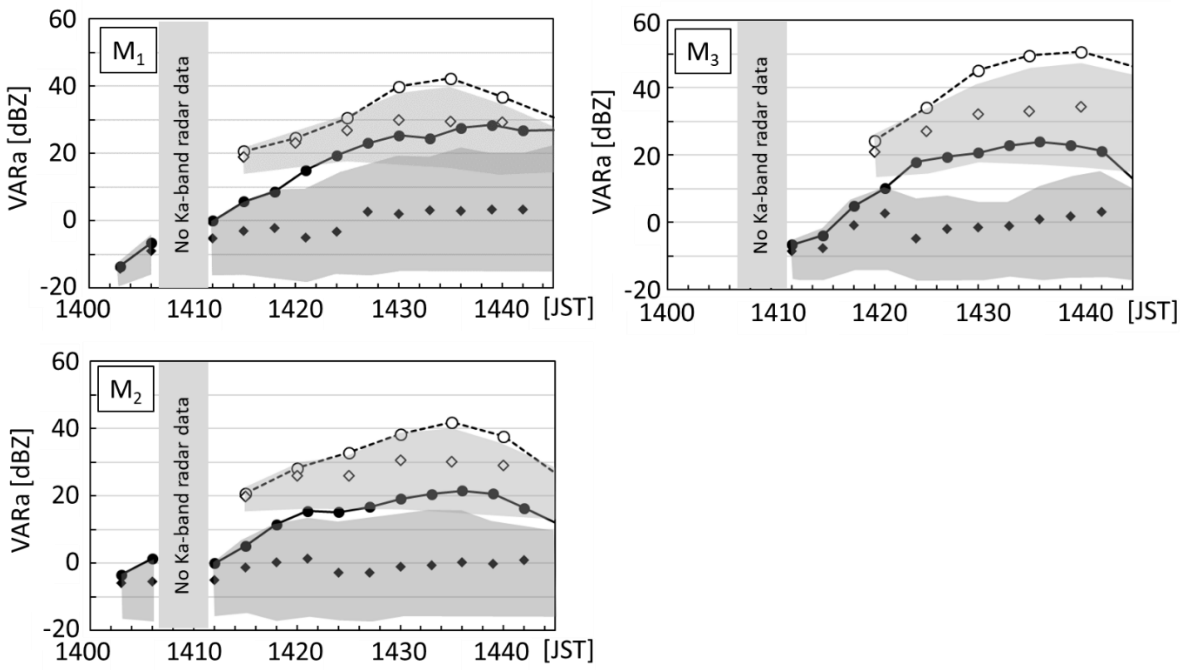

Fig. 10. Time series of VARa of MCEs (black circles) and MPEs (white circles) in CASE1. M1, M2, and M3 in the figure are MCEs identified in Fig. 9. Diamonds represent the 50th percentile of VAR within the MCE and MPE regions, and shaded areas represent the 25th and 75th percentiles. M3 may have existed during the outage of Ka-band radar (1409 JST).

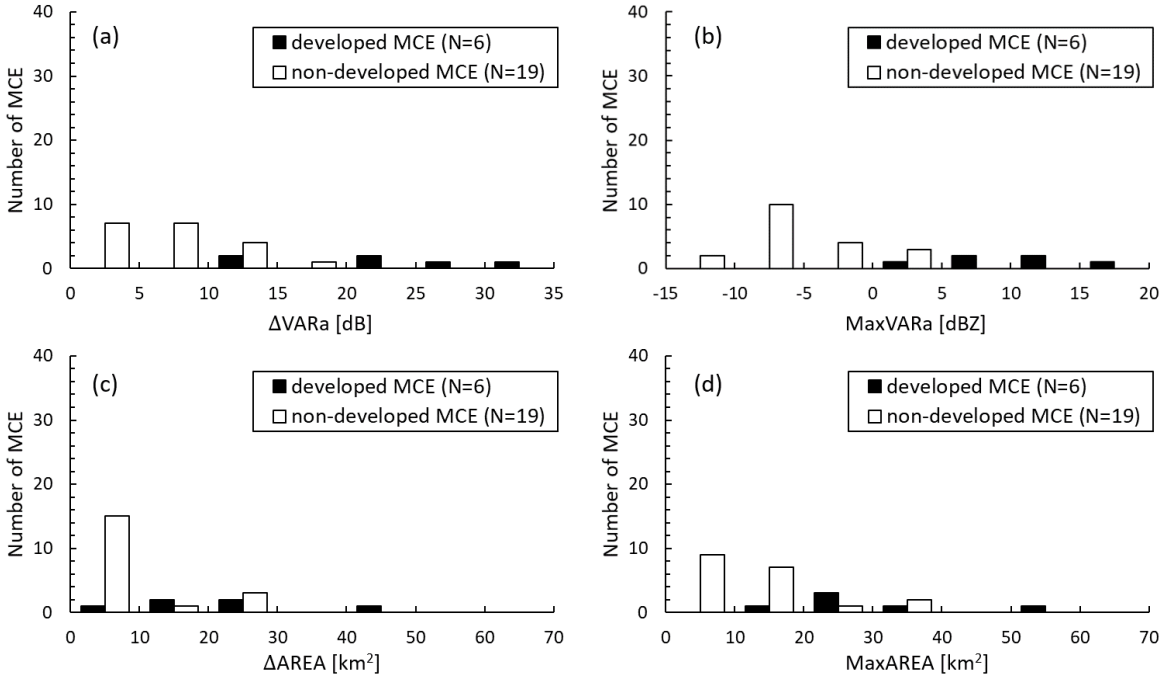

Fig. 11. Histograms of MCEs for (a) ΔVARa, (b) MaxVARa, (c) ΔAREA, and (d) MaxAREA for developed MCEs and non-developed MCEs for Δt = 15 minutes. N represents the number of corresponding MCEs.

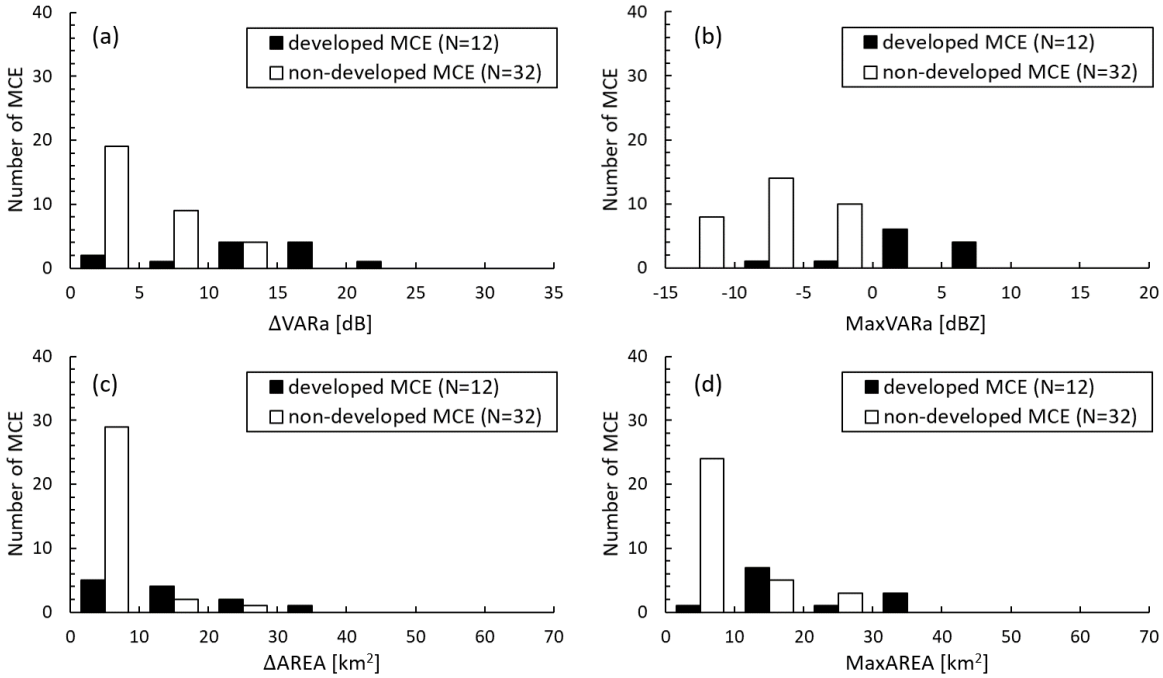

Fig. 12. Same as for Fig. 11, but for Δt = 9 minutes.

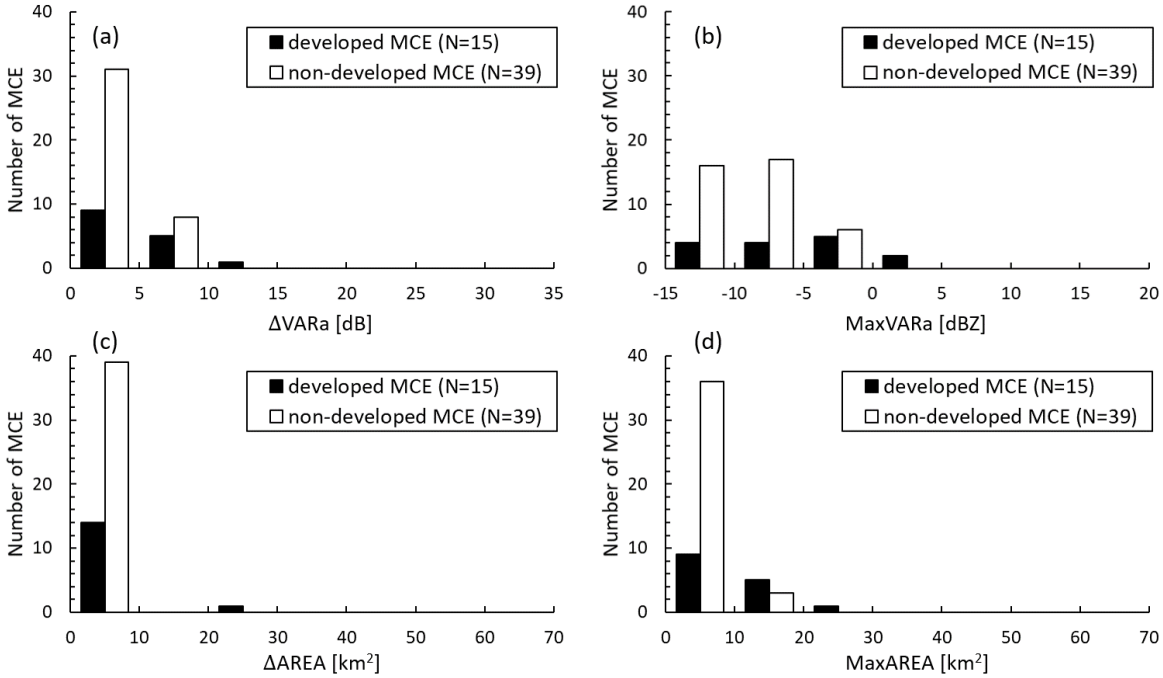

Fig. 13. Same as for Fig. 11, but for Δt = 3 minutes.

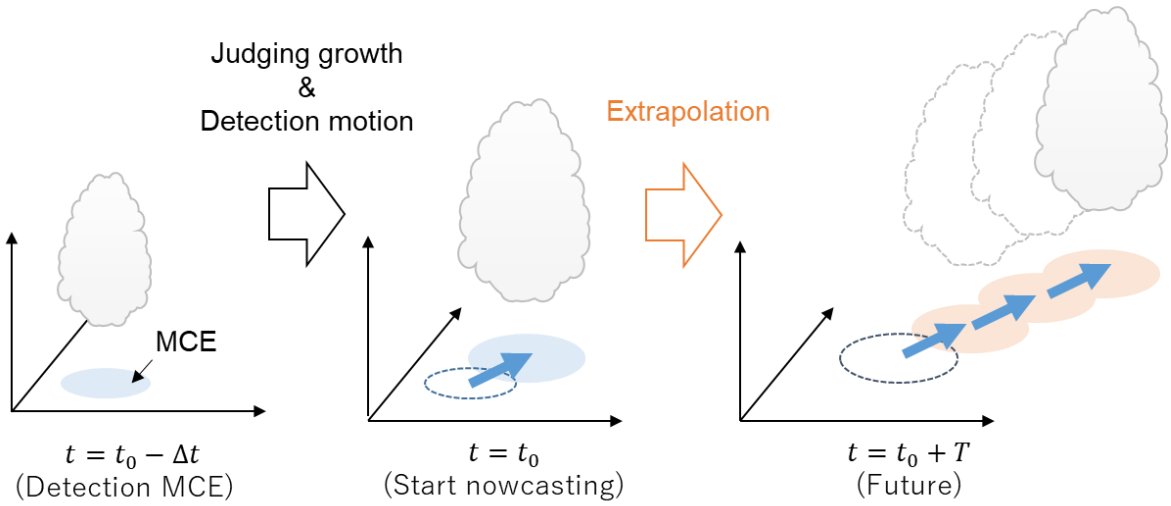

Fig. 14. Conceptual illustration of heavy rainfall forecast using the indicator developed in this study.

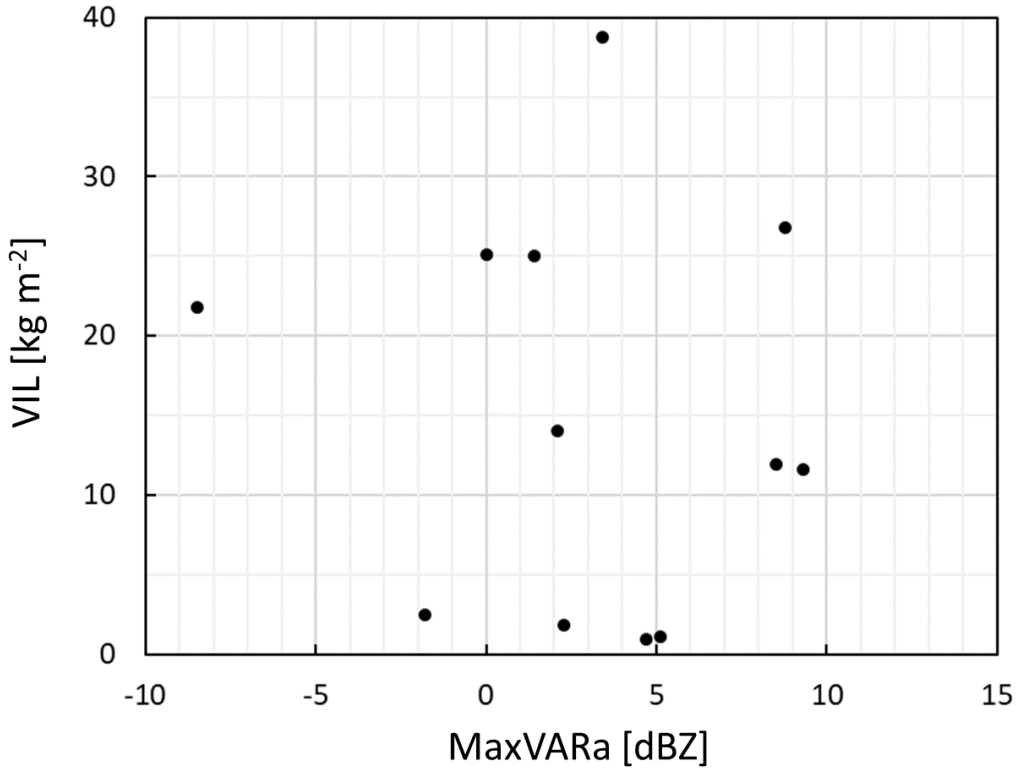

Fig. 15. Scatter plot of MaxVARa (Δt = 9 minutes) of developed MCEs and the maximum VIL of MPEs.